Imran, Mohamed & Mahendran, Mahen
(2021)
Numerical Modeling and Design of CFRP-Strengthened Short Steel Tubular Columns in Fire.
Journal of Structural Engineering (United States), *147*(4), Article number: 04021022.

https://doi.org/10.1061/(ASCE)ST.1943-541X.0002969

Numerical Modelling and Design of CFRP Strengthened Short Steel Tubular Columns in Fire

Mohamed Imran [a], Mahen Mahendran [b*]

[a] *Queensland University of Technology (QUT), Brisbane, QLD 4000, Australia, imrane12@yahoo.com*

[b] *Queensland University of Technology (QUT), Brisbane, QLD 4000, Australia, m.mahendran@qut.edu.au*

Abstract

This paper presents the details of a numerical study aimed at investigating the fire performance of CFRP strengthened short square hollow section (SHS) steel columns with and without an insulation system. Steady and transient state finite element (FE) models were developed to simulate the behaviour of CFRP strengthened columns exposed to uniform elevated temperatures and CFRP strengthened and insulated columns exposed to standard fire conditions, respectively. They were validated using the results of authors' experimental study. A detailed parametric study was then conducted using the validated steady state FE model to determine the influence of SHS steel grade and dimensions and CFRP strengthening configuration on the axial compression capacity deterioration at elevated temperatures, based on which suitable design equations were proposed to predict the elevated temperature axial compression capacity of CFRP strengthened columns. Fire resistance ratings (FRR) of CFRP strengthened and insulated SHS columns were determined based on the time-temperature profiles from heat transfer analyses and the load ratio versus critical temperature profiles developed from steady state FE analyses. In this study, two types of insulation materials (spray applied CAFCO 300 and intumescent paint) were investigated and both of them were found to provide satisfactory FRRs, where more than 60 min and 120 min FRRs were achieved for most columns with CAFCO 300 and intumescent paint, respectively. The modelling and design methods presented in this paper can be used to conduct fire safety designs of CFRP strengthened and insulated steel columns.

Keywords: Steel tubular columns; CFRP strengthening; Insulation; Fire performance; Finite element modelling; Fire Resistance Rating

1. Introduction

The widespread use of CFRP (Carbon Fibre Reinforced Polymer) over the past three decades as an external strengthening material for existing reinforced concrete columns has created a heightened interest towards using CFRP for steel column strengthening applications. Recent studies of steel columns strengthened with circumferential CFRP wraps have shown significant axial compression capacity enhancements and this success is attributed to many advantages associated with CFRP including high strength to weight ratio and high stiffness (Shaat and Fam 2006, Bambach et al. 2009 and Imran et al. 2018). However, this excellent strengthening material is subjected to one major limitation when CFRP composites soften at much lower temperatures (65-120°C), resulting in severe strength and stiffness reduction (Bisby 2003). This is because the adhesive, which is generally an epoxy, has a low glass transition temperature (typically in the above mentioned temperature range) and transfers from a hard solid state to a soft rubbery state, raising concerns over its performance in fire. In addition, these adhesives are combustible and may generate toxic smoke when they are exposed to elevated temperatures (Dai et el. 2015). Therefore, such concerns with respect to the fire performance of CFRP composites have hindered the use of CFRP strengthening for steel columns, which require certain fire resistance ratings (FRR).

The direct approach to assess the fire performance of CFRP strengthened steel columns and to obtain their FRR is to conduct a detailed experimental investigation. As part of an ongoing research study on the fire performance of CFRP strengthened steel columns, Imran and Mahendran 2020 conducted a series of experiments on CFRP strengthened SHS (Square Hollow Section) steel columns under steady state conditions, where a given column was heated to a pre-determined uniform temperature and tested until failure. Experimental results demonstrated that CFRP strengthened steel columns exhibit severe reduction to their axial compression capacity at temperatures beyond the glass transition temperature of the adhesive. In addition, the CFRP was deemed ineffective beyond 225°C and thus Imran and Mahendran 2020 emphasized the importance of an external insulation system to protect the CFRP strengthened steel columns to achieve satisfactory FRRs. Experimental studies on the fire resistance of externally insulated CFRP strengthened steel columns are limited and thus Imran and Mahendran 2020 conducted standard fire tests of CFRP strengthened SHS steel columns insulated with Vermiculite and Gypsum based spray applied insulation material (CAFCO 300) (Fig. 1), where more than 60 min of FRR was observed. In addition, detailed experimental studies of CFRP strengthened and insulated reinforced concrete (RC) columns have also shown that ameliorated FRRs can be achieved with appropriate external insulation systems (Bisby 2003, Kodur et al. 2006, Chowdhury et al. 2007 and Cree et al. 2012).

However, experimental studies undertaken to determine the FRRs are expensive and time consuming. Further, due to the limitations of experimental configurations, it is difficult to investigate the degradation mechanisms at local levels in an experiment. For instance, the behaviour of CFRP-steel interface is crucial for the global response of columns at elevated temperatures, but it cannot be understood well in an experiment (Dai et al. 2013). Therefore, finite element modelling was considered as an alternative to fire tests to assess the fire performance of CFRP strengthened steel columns.

Limited attempts have been made on modelling the behaviour of CFRP strengthened steel structural members at elevated temperatures (Al-Shawaf 2011 and, Proia and Matthys 2017). However, past studies have successfully modelled CFRP strengthened and insulated RC columns, and predicted their fire resistance and structural capacity reasonably well (Bisby et al. 2005, Liu et al. 2009, Kodur and Ahmed 2010 and Chowdhury et al. 2012). Hence, this research used finite element (FE) modelling to investigate the behaviour of CFRP strengthened short steel tubular columns (SHS) with and without an insulation system (Fig. 1) subject to local buckling failures at elevated temperatures. The developed FE models were validated using the results of Imran and Mahendran 2020 steady state tests and standard fire tests mentioned earlier. The validated models were then used in a detailed parametric study in which new design equations were proposed to determine the axial compression capacity of CFRP strengthened short SHS steel columns exposed to uniform elevated temperatures. Importantly, the effect of using external insulation was also investigated by varying the insulation type (CAFCO 300 and intumescent paint) and its thickness. Finally, the load ratio versus failure time/FRR curves were proposed for CFRP strengthened and insulated SHS steel columns subject to local buckling failures.

2. Finite element modelling

2.1. General

In this section, 3D FE models were first developed using ABAQUS/CAE FE software to simulate the two series of tests from authors' experimental study (Imran and Mahendran 2020) steady state tests of seven CFRP strengthened short SHS steel columns exposed to uniform elevated temperatures and two standard fire tests of CFRP strengthened and insulated short SHS steel columns. Both series of tests used Grade 350 100×100×2 mm SHS with a height of 300 mm, as the primary aim was to investigate the behaviour of steel columns subject to local buckling. The SHS columns were strengthened using 1T1L and 2T2L configurations in the first and second test series, respectively ('T' and 'L' refer to transverse and longitudinal CFRP layers and 1T1L means one layer of transverse and longitudinal CFRP). The average CFRP layer thickness was measured as 1.3 mm. The second test series columns were insulated with 30 mm of spray applied CAFCO

300 insulation. The insulation thickness of the fire protection material was determined based on a detailed heat transfer analysis (Imran et al. 2018).

Recently, FE models of CFRP strengthened short SHS steel columns at ambient temperature were developed and validated as part of this ongoing study (Imran et al. 2018). The same modelling strategies were used here. The FE model consisted of three parts representing the SHS steel column, adhesive and CFRP (Fig. 2). The insulation was not modelled as it does not contribute to the structural performance (Dai et al. 2015). Initially, the SHS steel column was modelled with shell elements with outward stacking direction. Then the mesh of the SHS column was solid offset to create both adhesive and CFRP layers. Both CFRP and adhesive layers were modelled for 284 mm height with an 8 mm gap at each end to simulate the experimental columns. All parts were meshed with 4 × 4 mm mesh size with five integration points. The contact between each layer was modelled by sharing the nodes with the base surface. Adhesive was only modelled between the steel and the first layer of CFRP to simulate the delamination between steel and CFRP because no inter-layer debonding was observed in the experiments.

Two independent reference nodes were created at each end of the column, and all peripheral nodes of the column edge were constrained to these reference nodes using beam type Multiple Point Constraints (MPC). These reference nodes were used to assign necessary boundary conditions, where all the translational and rotational degrees of freedom were fixed at the top and bottom ends except the loading directional movement at the top reference point (Fig. 2).

2.2. Material model and properties

2.2.1 Steel

The steel column was modelled as an elastic-plastic material with strain hardening. The stress-strain model proposed in Imran et al. 2018 was adopted using the measured ambient temperature mechanical properties (Table 1) and the elevated temperature mechanical property predictive equations. The engineering stress-strain values (σ and ε) were converted to true stress (σ_{true}) and true plastic strain (ε_{true}) values using Eqs. 1 and 2 in order to input in FE software, where E_0 is the elastic modulus. The thermal elongation values were obtained from EC3 Part 1.2 (EN 1993-1-2:2005).

$$\sigma_{true} = \sigma(1 + \varepsilon) \tag{1}$$

$$\varepsilon_{true} = \ln(1 + \varepsilon) - \frac{\sigma_{true}}{E_0} \quad (2)$$

2.2.2 Adhesive

The adhesive layer between steel and CFRP was modelled using coupled cohesive zone model based on traction separation law. In this model, the initial response of the adhesive (cohesive elements) is assumed to be linear until damage initiation (de Moura and Chousal 2006, and De Lorenzis et al. 2013).

Damage initiation is defined based on mixed mode failure criteria (QUADS), which considers both mode-I and mode-II loading effects (Eq. 3), where normal and shear tractions are denoted by t_n, t_s and t_t. σ_{max} and $\tau_{\max}$ are the tensile and shear strengths of the adhesive given by Eq. 4 (Teng et al. 2015). Damage is assumed to be initiated when the function reaches a value of one (SIMULIA ABAQUS 2011). The symbol $\langle\rangle$ signifies that the compressive stresses do not lead to damage and thus $\langle t_n \rangle$ is considered as zero if it is under compressive stress.

$$\left\{\frac{\langle t_n \rangle}{\sigma_{max}}\right\}^2 + \left\{\frac{t_s}{\tau_{\max}}\right\}^2 + \left\{\frac{t_t}{\tau_{\max}}\right\}^2 = 1 \quad (3)$$

$$\tau_{\max} = 0.9\sigma_{max} \quad (4)$$

Once the damage initiation criterion is met, material stiffness starts to degrade and damage evolution initiates. The damage evolution phenomenon was modelled using energy based linear softening approach in ABAQUS using Benzeggah-Kenane (BK) fracture energy based mixed mode law (Eq. 5) (Benzeggagh and Kenane 1996).

$$G_I + (G_{II} - G_I)\left(\frac{G_s}{G_t}\right)^{\eta} = G_n \quad (5)$$

where, G_n, G_s and G_t are work done in normal and shear directions while G_I and G_{II} are corresponding maximum fracture energies, which cause failures in normal and shear directions, respectively. Both G_I and G_{II} values are obtained from Alam et al. 2015 and the ambient temperature material properties of adhesive used in the model are given in Table 2. The η was taken as 1.55 (Benzeggagh and Kenane 1996).

With respect to the elevated temperature mechanical properties of adhesives, which are important to accurately simulate the fire behaviour of CFRP strengthened steel columns, this study obtained them by using the tensile strength (σ_{max}) and elastic modulus (E_a) reduction factors of the adhesive in Ferrier et al. [26] and the ambient temperature mechanical properties in Table 2.

Authors were unable to measure the mechanical properties of the adhesive due to limitations in the experimental set-up. The glass transition temperature of the adhesive used by Ferrier et al. 2016 is 76°C compared to 66°C used in this study (Imran et al. 2018), and thus it is considered to be reasonable to use their reduction factors in the FE analyses. As shown in Fig. 3, severe reductions in mechanical properties were reported at elevated temperatures, where approximately 90% and 95% of tensile strength and elastic modulus were lost at 80°C, respectively. Experimental results of Imran and Mahendran 2020 suggested that CFRPs are ineffective at 225°C and thus, both these properties were assumed to be zero at 225°C. Elevated temperature variations of k_{nn}, k_{ss}, and k_{tt} (elastic stiffness in normal and shear directions), and $\tau_{\max}$ (shear strength) were determined based on these reduction factors using the ambient temperature material properties. Elevated temperature G_I and G_{II} (maximum fracture energies in normal and shear directions) are primarily dependent on the tensile and shear strengths of the adhesive at a given temperature and thus these fracture energies were obtained based on the elevated temperature tensile and shear strength reduction factors, respectively (Teng et al. 2015).

2.2.3 CFRP

The tensile strength and elastic modulus of CFRP were determined by conducting tensile tests according to ASTM D3039/D3039M. Five CFRP tensile coupons were prepared in the fibre direction and tested with strain gauges attached on each side of the coupon (Imran et al. 2018). Table 3 shows the average tensile strength (T^L) and elastic modulus (E_{1C}) obtained from these tests.

In the FE model, the CFRP composite was modelled using lamina type elastic material and the damage of the composite was simulated using Hashin failure criteria (Hashin and Rotem 1973 and Hashin 1980). CFRPs display elastic-brittle damage behavior (damage is initiated without significant plastic deformation) and Hashin damage model has the ability to successfully predict the damage of these materials (Lesani et al. 2013). In this model, four different CFRP failure modes are considered: i. F_f^t- fibre rupture in tension, ii. F_f^c- fibre buckling in compression, iii. F_m^t- matrix cracking under transverse tension and shearing, and iv. F_m^c- matrix crushing under transverse compression and shearing. Following equations are used to determine the above criteria and a value of one or higher indicates that the damage initiation criterion has been met for a particular failure mode.

$$F_f^t = \left(\frac{\sigma_{11}}{T^L}\right)^2 + \alpha\left(\frac{\sigma_{12}}{S^L}\right)^2 \qquad (6)$$

$$F_f^c = \left(\frac{\sigma_{11}}{C^L}\right)^2 \quad (7)$$

$$F_m^t = \left(\frac{\sigma_{22}}{T^T}\right)^2 + \left(\frac{\sigma_{12}}{S^L}\right)^2 \quad (8)$$

$$F_m^c = \left(\frac{\sigma_{22}}{2S^T}\right)^2 + [\left(\frac{C^T}{2S^T}\right)^2 - 1]\frac{\sigma_{22}}{C^T} + \left(\frac{\sigma_{12}}{S^L}\right)^2 \quad (9)$$

σ_{11}, σ_{22} and σ_{12} are components of the stress tensor while 'α'is a coefficient that determines the contribution of shear stress and was taken as 1.0 (Hashin and Rotem 1973).

Damage evolution initiates once the damage criterion is met for a given failure mode and the damage is achieved when the energy dissipated is equal to the critical fracture energy of a given failure mode. Hence, the critical fracture energies for each failure mode has to be provided in the FE model.

Based on a detailed sensitivity study using available data on CFRP's fracture energies, the fracture energies given in Faggiani and Falzon 2010 were used as they were found to agree well with the experimental results of this study. Table 3 provides the fracture energies for each failure criterion. The compressive strength (C^L) of the commonly used CFRP varies from 9 to 60% of the tensile strength (Mostofinejad D and Moshiri 2015, and Nunes et al. 2016) and hence the longitudinal compressive strength of CFRP was assumed as 20% of the tensile strength. The transverse tensile/compressive and longitudinal/transverse shear strengths were assumed to be 10% of the tensile strength as many studies have shown that these values fall within the assumed range (Lesani et al. 2013 and, Faggiani and Falzon 2010). Poisson's ratio of the CFRP was taken as 0.33 (Kabir et al. 2016). In addition, viscosity coefficient of 0.0001 was used for damage stabilization purposes (Nunes et al. 2016).

The elevated temperature tensile and shear strengths of CFRP were determined using the reduction factors of Cree et al. 2015. Nguyen et al. 2011 provides the bond stiffness reduction of steel and CFRP interface with increasing temperature (Fig. 4). However, the glass transition temperature of the adhesive used by Nguyen et al. 2011 was 42°C compared to 66°C in this study (Imran et al. 2018). Therefore, the elastic modulus reduction factors of this study were shifted similarly to that of Nguyen et al. 2011, but the sudden reduction in elastic modulus was shifted to incorporate the difference in glass transition temperature (Fig. 4). Associated elevated temperature critical fracture energies were determined based on the tensile strength reduction factors.

2.3. Element types and analysis procedure

2.3.1 Steady state analysis

In the steady state analysis simulating the first series of Imran and Mahendran 2020 tests of CFRP strengthened short SHS columns, the temperature of columns was increased to the target temperature and then the load was increased until failure. The target temperatures were 20, 66, 81, 100, 150, 200 and 225°C (Table 4). S4R shell elements with reduced integration were used for SHS steel columns and CFRP layers were simulated using SC8R, 8-node quadrilateral general-purpose continuum shell elements with reduced integration and hourglass control. An 8-node three-dimensional cohesive element (COH3D8) was deployed to model the adhesive layer.

Initially, the associated material properties for a given temperature were assigned to all three parts. Then the elastic buckling analysis was performed to determine the critical buckling mode and load of the column, followed by nonlinear analysis using Riks method to determine the failure load and associated load-displacement behaviour. Nonlinear analysis incorporated geometric imperfections of the column, which were input by offsetting the primary coordinates with an amplitude of 0.006B in relation to the critical buckling mode, where B is the clear plate width (Schafer and Peköz 1998). It is to be noted that the initial geometric imperfections of the test columns were measured during the tests, but the measured maximum imperfection was less than 0.006B (Imran et al. 2018). The axial compression load was incrementally applied to the top reference node until failure.

2.3.2 Transient state analysis

Transient state analysis was conducted to simulate the second series of Imran and Mahendran 2020 standard fire tests of CFRP strengthened and insulated SHS columns. It was based on a sequentially coupled thermo-mechanical procedure (two steps), where the results of mechanical (structural) analysis depended on the heat transfer analysis. Initially, heat transfer analysis was performed to obtain the time-temperature variations of CFRP and steel surfaces. Then the structural analysis was performed using the results of heat transfer analysis.

Heat transfer modelling of CFRP strengthened and insulated steel columns exposed to standard fire was conducted in the authors' recent study. The measured thermal properties of CFRP and insulation were used here, and the model considered the effect of conduction, radiation and convection as primary heat transfer modes. Using the developed heat transfer model, the time-temperature profiles of CFRP and steel surfaces of experimental columns were obtained (Fig. 5), which agreed well with experimental time-temperature profiles reported in (Imran and Mahendran

2020). As seen in Fig. 5, the use of insulation delayed the temperature rise on CFRP and steel surfaces. The time-temperature profiles of CFRP and steel surfaces were then imposed as boundary conditions to obtain the structural response in transient state analysis.

CFRP layers and steel column were modelled using 8-node thermally coupled quadrilateral in-plane general-purpose continuum shell elements with reduced integration and hourglass control (SC8RT), and 4-node thermally coupled shell elements (S4RT), respectively. An 8-node 3D cohesive element (COH3D8) was deployed to model the adhesive layer.

Two standard fire tests were conducted with constant applied loads of 79 and 115 kN to represent load ratios of 0.2 and 0.3, which were used in the structural analysis. Initially, temperature dependant material properties were assigned to the adhesive, CFRP and steel sections. Elastic buckling analyses were performed then to determine the critical buckling mode and load followed by loading of the column at ambient temperature. Non-linear analysis was conducted using the coupled temperature-displacement method to determine the failure time. Geometric imperfections were included using a similar approach to that of steady state analysis.

3. Validation

3.1. Steady state analysis

For validation purposes, the results from steady state FE analysis were compared with steady state experimental results in Fig. 6 and Table 4. Fig. 6 compares the load-displacement curves obtained from FEA and experiments, where SHS columns are denoted according to the temperature to which they were exposed to and ‘SS’ refers to steady state conditions. Although the failure loads from experiments and FE analyses show a very good agreement, there is a difference in the axial stiffness. This was attributed to the difficulties in the axial displacement measurements in the elevated temperature test set-up. The LVDTs used to measure the axial displacements of test columns had to be located below the furnace and thus the measured axial displacements also included the axial shortening of test rig components (compressed cement fibre sheets, loading shafts and end plates), which influenced the experimental stiffness values. Both FEA and experimental results show a decreasing trend in elastic stiffness and ultimate load with increasing temperature. Moreover, comparatively similar post-failure load-displacement variation is observed in both FEA and experimental curves.

Apart from Column SS-20, which failed in yielding, all the columns underwent local buckling failures and FEA were able to predict those failures quite well. Fig. 7 shows the failure mode comparisons of columns SS-20 and SS-100. Table 4 compares the failure loads obtained from experiments and FEA, which demonstrates a good agreement with the overall mean and coefficient of variation (COV) of 1.019 and 0.024 for the ratios between FEA and experimental failure loads. Therefore, it is concluded that the developed FE models are capable of simulating the elevated temperature (steady state) behaviour of CFRP strengthened steel columns with good accuracy.

3.2. Transient state analysis

The results of transient state FE analyses were compared with the standard fire test results of SF-0.2 and SF-0.3 columns (SF refers to Standard Fire) for validation purposes. Figs. 8 and 9 show the comparison of load and axial displacement curves of SF-0.2 and SF-0.3 columns, respectively. Both columns were strengthened with CFRP and insulated with 30 mm of spray applied CAFCO 300 insulation. Column SF-0.2, which was subjected to 0.2 load ratio, failed after 61 min of standard fire exposure and FEA predicted its failure time as 55 min. On the other hand, Column SF-0.3, which was subjected to 0.3 load ratio, failed at 50 min and FEA predicted its failure time as 52 min. Hence, the transient state FE models are considered capable of predicting the failure time and behaviour with good accuracy.

Both experimental axial displacement profiles showed a gradual increase in axial displacement after the failure of the column. However, the predicted axial displacement variations of FEA showed a gradual increase in axial displacement from about 30 min, which might be due to the expansion of steel columns at elevated temperature. The load was gradually released during the fire test so that the applied load was maintained. As a result, the deformation due to the expansion of steel columns in experimental axial displacement measurements is negated to some extent and this phenomenon might be the reason for the slight variations in experimental and FEA axial displacement profiles. In addition, both experiments and FEA predicted the local buckling failures as shown in Fig. 10. Therefore, it is concluded that the developed transient state FE models are capable of simulating the behaviour of standard fire exposed CFRP strengthened and insulated steel columns.

4. Parametric study

The validated steady state FE models were used to conduct a detailed parametric study to investigate the effects of SHS section sizes, steel grade, CFRP strengthening configuration and temperature. Four SHS (100×100×2, 200×200×2, 200×200×5 and 350×350×8) with slender plate elements were selected to include a wide range of slenderness ratios. These four SHS were chosen based on an initial study that was undertaken to determine the most suitable commercially available sections that are prone to local buckling. All the SHS column sections used in this study are slender and are expected to undergo local buckling failures. Both Grade 350 and Grade 450 steels were considered. The SHS column heights were taken as three times the clear width of the section to allow the development of three half wave local buckles. Generally, four CFRP strengthening configurations were investigated for each SHS column: 1T, 1L, 1T1L and 2T2L. Furthermore, the columns were exposed to seven steady state temperatures (20, 66, 81, 100, 150 and 200°C) to investigate the axial compression capacity deterioration with increasing temperature. The experimental results of Imran and Mahendran 2020 showed that CFRP is totally ineffective at 225°C and thus the axial compression capacity beyond 225°C was considered equal to that of the unstrengthened bare steel column at the same temperature.

The same FE modelling approaches discussed in Section 2.3.1 were used in the parametric study. The ambient temperature yield strength was taken as 350 or 450 MPa, with an elastic modulus of 210 GPa. The elevated temperature mechanical properties and stress-strain models were obtained using the predictive equations given in Imran et al. 2018. The nominal CFRP thickness was taken as 1.24 mm.

Tables 5 to 8 present the temperature dependent axial compression capacities ($P_{u,T}$) obtained from the parametric study for Grade 450 SHS sections because of space limitations. However, the results of both Grade 350 and Grade 450 SHS are plotted in Figs. 11 to 14. At ambient temperature, CFRP strengthening provides significant enhancement to the axial compression capacity and the capacity of a given SHS column increases with the number of CFRP layers. In addition, longitudinal CFRP layers were found to be performing slightly better than the transverse CFRP layers. However, when these columns are exposed to elevated temperatures, especially for temperatures beyond the glass transition temperature of the adhesive, they show a significant capacity reduction and consequently a large reduction in the load ratio ($\frac{P_{u,T}}{P_{u,20}}$). Load ratio, which can also be termed as the capacity reduction factor, refers to the ratio between the axial compression capacity at a given temperature to that at ambient temperature.

Figs. 11 to 14 show the variation of load ratio with temperature for both Grade 350 and Grade 450 SHS columns. All the unstrengthened bare steel columns show similar behaviour with increasing temperature and the load ratio/capacity reduction factor versus temperature variation was found to be independent of SHS dimensions and steel grade. In contrast, the load ratio versus temperature profiles of CFRP strengthened columns were found to be dependent on CFRP strengthening configuration, SHS dimensions and steel grade. Higher reductions were observed at a given temperature when the number of CFRP layers was increased for a given SHS column. For instance, Grade 450 100×100×2 SHS column strengthened with 1T1L CFRP configuration shows a capacity reduction factor of 0.57 at 200°C compared to 0.76 of 1T CFRP configuration (Fig. 11). This is because, 1T1L CFRP configuration exhibits higher axial compression capacity enhancement at ambient temperature and as a result suffers a higher reduction at elevated temperatures.

In general, most of the CFRP strengthened Grade 450 SHS columns showed slightly higher capacity reductions with increasing temperature compared to Grade 350 SHS columns. CFRP strengthened columns show higher capacity increments with increasing steel grade and thus are vulnerable to higher capacity reductions at elevated temperatures. Similarly, more slender SHS sections are prone to high capacity reductions at elevated temperatures. For example, Grade 450 200×200×2 SHS column with a slenderness ratio (λ_e) of 129 and a 2T2L CFRP configuration showed a capacity reduction factor of 0.36 (Fig. 12) at 200°C compared to 0.66 of the same column with a λ_e of 47 (Fig. 13). Slenderness ratio (λ_e) is given by Eq. 10, where b, t and f_y are clear section width, thickness and yield strength, respectively.

$$\lambda_e = \frac{b}{t}\sqrt{\frac{f_y}{250}} \tag{10}$$

5. Design equations

In this section, two design approaches given in Imran et al. 2018 for ambient temperature conditions are modified to predict the elevated temperature axial compression capacity of CFRP strengthened short SHS columns subject to local buckling.

5.1. Modified model of Bambach et al. 2009

The temperature dependant axial compression capacity is given by,

$$P_{u,T} = 4\,\rho\, b\, t\, f_{y,T} + A_r\, f_{y,T} \tag{11}$$

where, b is the clear width determined based on width (b_w) and corner radius (r) of the SHS steel section using Eq. 12. t and A_r refer to thickness and rounded corner area (determined based on gross area of the section (A_g) using Eq. 13) of the SHS, respectively. Temperature (T in °C) dependent yield strength ($f_{y,T}$) is given by Eq. 14 (Imran et al. 2018), where $f_{y,20}$ is the ambient temperature yield strength. Effective width factor of the composite section (ρ), which is a function of the plate slenderness ratio ($\lambda_{C,T}$), is given by Eq. 15.

$$b = b_w - 2\,r \tag{12}$$

$$A_r = A_g - 4\,b\,t \tag{13}$$

$$\frac{f_{y,T}}{f_{y,20}} = \frac{1}{0.992 + 0.0063 \times e^{\frac{T}{105}}} \tag{14}$$

$$\rho = \frac{1 - \frac{0.22}{\lambda_{C,T}}}{\lambda_{C,T}} \tag{15}$$

$$\lambda_{C,T} = \sqrt{\frac{f_{y,T}}{f_{cr,T}}} \tag{16}$$

$f_{cr,T}$ and $P_{cr,T}$ are the temperature dependant elastic buckling stress and load of the CFRP strengthened steel column given by Eqs. 17 to 22. The elastic buckling coefficient, k, was taken as 4.0 for stiffened elements. D_t is the flexural rigidity of the composite section determined based on Pister and Dong (1959).

$$f_{cr,T} = \frac{k\,\pi^2\,D_t}{t\,b^2} \tag{17}$$

$$P_{cr,T} = A_g\,f_{cr,T} \tag{18}$$

$$D_t = \frac{D_1 D_3 - {D_2}^2}{D_1} \tag{19}$$

$$D_1 = \frac{E_{S,T}\,t}{1 - {\upsilon_S}^2} + \frac{E_{CE,T}\,(t_{Total} - t)}{1 - {\upsilon_C}^2} \tag{20}$$

$$D_2 = \frac{E_{S,T}\,t^2}{2(1 - {\upsilon_S}^2)} + \frac{E_{CE,T}\,({t_{Total}}^2 - t^2)}{2(1 - {\upsilon_C}^2)} \tag{21}$$

$$D_3 = \frac{E_{S,T}\,t^3}{3(1 - {\upsilon_S}^2)} + \frac{E_{CE,T}\,({t_{Total}}^3 - t^3)}{3(1 - {\upsilon_C}^2)} \tag{22}$$

t_{Total} is the total thickness of the CFRP strengthened steel section given by Eq. 23 in terms of steel thickness (t), individual CFRP layer thickness (t_C), and the number of transverse (N_{Tr}) and longitudinal (N_L) CFRP layers. $E_{s,T}$ is the temperature dependant elastic modulus of steel given by Eq. 24 based on the ambient temperature elastic modulus ($E_{s,20}$) (Imran et al. 2018). Equivalent stiffness of the CFRP, $E_{CE,T}$, is given by Eq. 25. Temperature dependant elastic modulus of CFRP in the fibre direction ($E_{1C,T}$) was obtained based on the reduction factors given in Fig. 4. The proportioning factor (ξ) factor, which takes into account the effect of transverse CFRP layers, was taken as 0.8 for the given type of CFRP used. It is to be noted that the proportioning factor is a characteristic of the CFRP composite used in column strengthening and thus may vary depending on the CFRP type.

$$t_{Total} = t + t_C\,(N_L + N_{Tr}) \tag{23}$$

$$\frac{E_{s,T}}{E_{s,20}} = \frac{1}{0.991 + 0.0075 \times e^{\frac{T}{114}}} \tag{24}$$

$$E_{CE,T} = \frac{N_L\ E_{1C,T} + \xi\ N_{Tr}\ E_{1C,T}}{N_L + N_{Tr}} \tag{25}$$

Tables 5 to 8 show the axial compression capacities of CFRP strengthened short SHS columns exposed to elevated temperatures ($P_{u,T,th}$) obtained from the proposed design equations and compare them with those obtained from FEA ($P_{u,T}$). The proposed design equations are found to be predicting the elevated temperature axial compression capacities accurately, where the mean and COV values of the ratios between theoretical and FEA capacities are 0.99 and 0.076, respectively. The capacity reduction factor for the proposed design equations was calculated as 0.88 based on the recommended AISI procedure 2007. The capacity reduction factors in AS 4100:1998 and AS/NZS 4600:2005 are 0.90 and 0.85, respectively, and thus a capacity reduction factor of 0.85 is recommended for use with the developed design equations.

5.2. Direct Strength Method (DSM)

Imran et al. 2018 proposed a design approach based on direct strength method to determine the ambient temperature axial compression capacities of CFRP strengthened short SHS steel columns. Therefore in this paper, the applicability of those equations to predict the elevated temperature axial compression capacities was investigated (Eqs. 26 to 29).

Initially, $\frac{P_{u,T}}{Py,T}$ ratios were obtained using the parametric study FEA results based on the temperature dependent yield load $\left(P_{y,T}\right)$ of the short SHS steel column (Tables 5 to 8), calculated based on Eq. 29. Then these ratios were plotted against the corresponding slenderness ratios of the composite section (λ_T) given by Eq. 26. Fig. 15 shows both ambient and elevated temperature CFRP strengthened columns' variations of $\frac{P_u}{Py}$ versus λ_T ($\frac{P_{u,T}}{Py,T}$ for elevated temperature conditions). $\frac{P_{u,T}}{Py,T}$ ratios for elevated temperature conditions show slightly smaller values for high slenderness ratios compared to the DSM equations developed for ambient temperature conditions. Therefore, a new set of DSM design equations was proposed to predict the axial compression capacities of CFRP strengthened columns exposed to elevated temperatures (Eqs. 27 to 29). The temperature dependent critical buckling load of CFRP strengthened short SHS column ($P_{cr,T}$) can be obtained using Eq. 18 or alternatively any FE software may be utilized.

$$\lambda_T = \sqrt{\frac{P_{y,T}}{P_{cr,T}}} \tag{26}$$

$$For\ \lambda_T \leq 0.52, \qquad P_{u,T} = 1.2P_{y,T} \tag{27}$$

$$For\ \lambda_T > 0.52, \qquad P_{u,T} = \left[1 - 0.20\left(\frac{P_{cr,T}}{P_{y,T}}\right)^{0.53}\right]\left(\frac{P_{cr,T}}{P_{y,T}}\right)^{0.53} P_{y,T} \tag{28}$$

$$P_{y,T} = A_g\, f_{y,T} \tag{29}$$

The accuracy of the developed elevated temperature DSM based design equations was investigated by comparing the results from FEA. The mean and COV of the ratios between the DSM and FEA predictions were found to be 1.03 and 0.045, respectively. The capacity reduction factor based on the recommended AISI procedure 2007 was obtained as 0.94, which shows the suitability of the proposed equations to predict the elevated temperature axial compression capacity of CFRP strengthened short SHS steel columns. Hence, a capacity reduction factor of 0.90 is recommended for use with the proposed DSM equations.

6. FRR Prediction

The results of the parametric study showed that the CFRP strengthened steel columns are prone to severe strength reduction at elevated temperatures and their fire performance is a serious concern. In addition, Figs. 11 to 14 show that the elevated temperature performance of CFRP strengthened columns is worse than that of the unstrengthened bare steel column because the critical failure temperature for a given load ratio is always lower for CFRP strengthened columns. Therefore, these results demonstrate the need to have an external insulation layer to protect the CFRP and to achieve higher Fire Resistance Ratings (FRR), where FRR refers to the time period that a given column withstands the standard fire exposure under the applied load without a structural failure. Hence, an investigation was conducted to determine the FRRs of CFRP strengthened and insulated SHS steel columns exposed to standard fire conditions. Transient state FE analyses simulate the fire tests closely and provide the failure times (FRR) of CFRP strengthened and insulated SHS steel columns, but they require extensive memory and computing time. Hence steady state analyses, which are less time consuming and provide almost similar results, were used to determine the failure times.

Initially, the critical temperature, the maximum steel temperature that a given column can withstand under a particular load ratio, was determined using the load ratio versus temperature variations (Figs. 11 to 14). In this investigation, steel hollow section columns will be experiencing similar temperatures along hollow section webs and flanges during fire events, ie. approximately uniform temperature conditions. Thus, considering the maximum temperature as the critical temperature is considered to be reasonable. The critical temperature of Grade 450 350×350×8 SHS column strengthened with 2T2L CFRP configuration was 402°C under 0.6 load ratio (Fig. 14). Tables 9 to 12 show the critical temperatures of Grade 450 SHS columns for different load ratios. It was observed that the critical temperatures for bare short SHS columns were almost similar for a given load ratio and they are independent of the section dimensions. However, the critical temperatures for CFRP strengthened columns depend on the SHS section dimensions, steel grade and CFRP configuration. Once the critical temperature for a given column is found, the FRR or the failure time can be determined if the time-temperature profile of the steel surface is known. Time-temperature profiles of steel surface can be determined by conducting a heat transfer analysis as described in Imran et al. 2018.

Generally, spray applied insulation materials and intumescent paints are used to protect steel columns and this study considered the effect of both these insulation materials in protecting the CFRP strengthened SHS steel columns. Fig. 16 shows the time-temperature profiles of steel surfaces obtained for standard fire exposed CFRP strengthened SHS steel columns with spray applied CAFCO 300 insulation of three different thicknesses (20, 30 and 40 mm).

A similar heat transfer modelling procedure was used in this study considering the intumescent paint as the insulation layer. The same modelling strategies described in Imran et al. 2018 were used with the thermal properties of intumescent paint obtained from Podolski 2017. Constant specific heat and density values of 1000 J/kgK and 100 kg/m^3 were used. The effective thermal conductivity variation, which considers the expansion of paints at elevated temperatures, as given in Podolski 2017 was used (Fig. 17). Three intumescent paint thicknesses (1.25, 2.5 and 5 mm) were considered and the obtained time-temperature profiles of steel surfaces of standard fire exposed CFRP strengthened SHS columns protected with intumescent paints are shown in Fig. 16.

In general, both insulation materials show their capability of keeping the steel surface temperature at lower levels. However, steel surface temperature goes beyond the glass transition temperature of the adhesive (generally around 65 to 120°C) within a shorter period of time (Fig. 16) when using intumescent paints compared to CAFCO 300 and thus the effect of CFRP will be diminished soon if intumescent paints are used. But intumescent paints maintain the steel surface temperatures at lower levels even with lower thicknesses than the CAFCO 300 for the rest of the fire exposure.

The time-temperature profiles in Fig. 16 and the critical temperatures in Tables 9 to 12 were then used to determine the failure times/FRRs of CFRP strengthened and insulated steel columns. For example, Grade 450 350×350×8 SHS column strengthened with 2T2L CFRP configuration under 0.6 load ratio, which had a critical temperature of 402°C, gives a FRR of 58 min with 40 mm of CAFCO 300 and 115 min with 5 mm of intumescent paint (Fig. 16). Similarly, FRR for each configuration was determined. Figs. 18 to 21 and Figs. 22 to 25 show the load ratio versus FRR/failure time variations of CFRP strengthened Grade 450 SHS columns insulated with CAFCO 300 and intumescent paint, respectively. The insulation thickness is shown in the legend next to the CFRP configuration. These load ratio versus FRR profiles can be used to obtain the FRR/failure time of a given CFRP strengthened and insulated SHS column under any load ratio. The FRR of a given column increases with increasing insulation thickness whereas it reduces for SHS columns strengthened with higher number of CFRP layers.

Generally, the columns insulated with intumescent paints show higher FRRs than those insulated with CAFCO 300 even with a small insulation thickness. For example, Grade 450 100×100×2 SHS column strengthened with 1T1L CFRP configuration and insulated with 40 mm CAFCO 300 shows a FRR of 60 min under 0.4 load ratio compared to 122 min using 5 mm thick intumescent paint (Figs. 18 and 22). However, the columns insulated with intumescent paints show very low

FRRs for higher load ratios due to the initial high temperature rise in steel surfaces when intumescent paints are used (Fig. 16).

All the columns with load ratios below 0.6 satisfy the 30 min FRR requirement in NCC 2019 when insulated with at least 30 mm of CAFCO 300 insulation. FRRs of more than 60 min are observed for most columns with load ratios below 0.4 and insulated with 40 mm of CAFCO 300 insulation. On the other hand, 5 mm intumescent paint gives more than 2 hr FRRs for most columns subject to load ratios below 0.4. Apart from a few exceptions, Figs. 22 to 25 show that even a 2.5 mm of intumescent coating provides 30 min FRR for most of the columns with load ratios below 0.6. These results show that a suitable insulation system can provide the FRR required by various design standards.

7. Conclusions

This paper has presented the details of a numerical study conducted to investigate the fire performance of CFRP strengthened short SHS steel columns with and without an insulation system. Steady state FE models were developed to simulate the axial compression behaviour of CFRP strengthened SHS steel columns exposed to uniform elevated temperatures while transient state FE models were developed to simulate the behaviour of CFRP strengthened and insulated SHS steel columns under standard fire conditions. The developed FE models were validated using the corresponding experimental results of authors' recent study and then used in a detailed parametric study. The results showed a severe reduction in the axial compression capacity when the temperature was increased beyond the glass transition temperature of the adhesive. The rate of axial compression capacity reduction was found to be dependent on the steel grade, SHS dimensions and CFRP configuration. The authors' modified model of Bambach et al. 2009 for the ambient temperature axial compression capacity was shown to be capable of predicting the elevated temperature capacities of CFRP strengthened short SHS steel columns by using appropriate elevated temperature mechanical properties. A design approach based on DSM was also presented in this paper.

FRR/failure times of CFRP strengthened and insulated steel columns exposed to standard fire were determined using the load ratio versus temperature curves obtained using steady state analyses and the time-temperature curves obtained using heat transfer analyses. Both types of insulations considered in this study, vermiculite and gypsum based CAFCO 300 insulation and intumescent paint, provided satisfactory FRRs by protecting the CFRP strengthened columns in fire, where more than 60 min and 120 min of FRRs were observed for many columns insulated with CAFCO 300 and intumescent paint, respectively. Therefore, it is concluded that FRRs required by various design standards can be achieved for CFRP strengthened short SHS steel columns by using a suitable fire insulation system. The procedure presented in this paper can be used to determine the required insulation type and thickness for any CFRP strengthened short steel column depending on the required FRR.

8. Data Availability

Some or all data, models, or code generated or used during the study are available from the corresponding author by request. They include the results from experiments and finite element analyses and the processed results.

9. Acknowledgements

The authors would like to express their gratitude to Queensland University of Technology (QUT) for providing the research facilities required to conduct the work reported in this paper. They also would like to thank Dr Poologanathan Keerthan's support to the first author in the initial stages of this study.

List of symbols

A_g - gross area of steel section

A_r - rounded corner area of steel section

b - clear width of steel section

b_w - width of steel section

C^L - compressive strength of CFRP in longitudinal direction

C^T - compressive strength of CFRP in transverse direction

D_t - flexural rigidity of composite section

E_a - elastic modulus of adhesive

E_s - elastic modulus of steel

$E_{S,T}$ - temperature dependent elastic modulus of steel

E_{1C} - elastic modulus of CFRP in longitudinal direction

E_{2C} - elastic modulus of CFRP in transverse direction

$E_{1C,T}$ - temperature dependent elastic modulus of CFRP in transverse direction

$E_{1C,L}$ - temperature dependent elastic modulus of CFRP in longitudinal direction

$E_{CE,T}$ - temperature dependent equivalent stiffness of CFRP

$f_{y,20}$ - yield strength of steel at ambient temperature

$f_{y,T}$ - temperature dependent yield strength of steel

$f_{cr,T}$ - temperature dependent elastic buckling stress

F_f^t - fibre rupture in tension

F_f^c - fibre buckling in compression

F_m^t - matrix cracking under transverse tension and shearing

F_m^c - matrix crushing under transverse compression and shearing

G_I - fracture energy of Mode I failure

G_{II} - fracture energy of Mode II failure

G_{ft} - fracture energy for fibre tension

G_{fc} - fracture energy for fibre compression

G_{mt} - fracture energy for matrix tension

G_{mc} - fracture energy for matrix compression

k - elastic buckling coefficient

N_L - number of longitudinal CFRP layers

N_{Tr} - number of transverse CFRP layers

$P_{u,20}$ - axial compression capacity at ambient temperature

$P_{u,T}$ - temperature dependent axial compression capacity

$P_{y,T}$ - temperature dependent yield load

$P_{u,T,th}$ - temperature dependent theoretical axial compression capacity

$P_{cr,T}$ - temperature dependent critical buckling load

S^L - shear strength of CFRP in longitudinal direction

S^T - shear strength of CFRP in transverse direction

t - thickness of steel section

t_C - CFRP layer thickness

T_g - glass transition temperature of adhesive

T^L - tensile strength of CFRP in longitudinal direction

T^T - tensile strength of CFRP in transverse direction

t_{Total} - total thickness of composite section

σ - engineering stress

σ_{true} - true stress

σ_{max} - tensile strength of adhesive

ε - engineering strain

ε_{true} - true strain

$\tau_{\max}$ - shear strength of adhesive

α - coefficient that determines the contribution of shear stress

λ_e - slenderness ratio of steel column

$\lambda_{C,T}$ - plate slenderness ratio

λ_T - slenderness ratio of composite section

ρ - effective width factor of composite section

ξ - proportioning factor

References

Al-Shawaf, A. 2011. "Modelling wet lay-up CFRP–steel bond failures at extreme temperatures using stress-based approach". *International Journal of Adhesion and Adhesives*. 31: 416-28.

Alam, M. I., S. Fawzia, and X.M. Liu. 2015. "Effect of bond length on the behaviour of CFRP strengthened concrete-filled steel tubes under transverse impact". *Composite. Structures* 132: 898-914.

American Iron Steel Institute (AISI) 2007. *North American Specification for the Design of Cold-formed Steel Structural Members*. Washington, DC, USA: AISI.

ASTM D3039/D3039M − 14 -Standard Test Method for Tensile Properties of Polymer Matrix Composite Materials, West Conshohocken, PA 19428-2959. USA.

Benzeggagh, M. L., and M. Kenane. 1996. "Measurement of mixed-mode delamination fracture toughness of unidirectional glass/epoxy composites with mixed-mode bending apparatus". *Composites Science and Technology*. 56(4): 439-449.

Bambach, M. R., H. H. Jama, and E. Elchalakani E. 2009. "Axial capacity and design of thin-walled steel SHS strengthened with CFRP". *Thin-Walled Structures*. 47: 1112-21.

Bisby L. A. 2003. *Fire behaviour of fibre-reinforced polymer (FRP) reinforced or confined concrete.* PhD thesis. Kingston, Canada: Queens University.

Bisby, L. A., M. F. Green, and V. K. R. Kodur. 2005. "Modeling the Behaviour of Fibre Reinforced Polymer-Confined Concrete Columns Exposed to Fire". *Journal of Composites for Construction*. 9: 15-24.

Chowdhury E. U., L. A. Bisby, M. F. Green, and V. K. R. Kodur. 2007. "Investigation of insulated FRP-wrapped reinforced concrete columns in fire". *Fire Safety Journal*. 42: 452-60.

Chowdhury, E. L. Bisby, M. Green, N. Bénichou, and V. K. R. Kodur. 2012. "Heat transfer and structural response modelling of FRP confined rectangular concrete columns in fire". *Construction and Building Materials*. 32: 77-89.

Cree, D., E. U. Chowdhury, M. F. Green, L. A. Bisby, and N. Bénichou. 2012. "Performance in fire of FRP-strengthened and insulated reinforced concrete columns". *Fire Safety Journal*. 54: 86-95.

Cree, D., T. Gamaniouk, M. L. Loong, and M. F. 2015. "Green. Tensile and Lap-Splice Shear Strength Properties of CFRP Composites at High Temperatures". *Journal of Composites for Construction*. 19: 4014043.

Dai, J-G, W. Y. Gao, and J. G. Teng. 2013. "Bond-Slip Model for FRP Laminates Externally Bonded to Concrete at Elevated Temperature". *Journal of Composites for Construction*. 17: 217-28.

Dai, J-G, W. Y. Gao, and J. G. Teng. 2015. "Finite Element Modeling of Insulated FRP-Strengthened RC Beams Exposed to Fire". *Journal of Composites for Construction*. 19: 4014046.

De Lorenzis, L., D. Fernando, and J. G. Teng. 2013. "Coupled mixed-mode cohesive zone modeling of interfacial debonding in simply supported plated beams". *International Journal of Solids and Structures.* 50(14-15): 2477-2494.

de Moura, M. F. S. F., and J. A. G. Chousal. 2006. "Cohesive and continuum damage models applied to fracture characterization of bonded joints". *International Journal of Mechanical Sciences* 48(5): 493-503.

EN 1993-1-2. 2005. Eurocode 3: *Design of Steel Structures. Part 1-2: General Rules- Structural Fire Design*. Brussels, Belgium: European Committee for Standardization.

Faggiani, A., and B. G. Falzon. 2010. “Predicting low-velocity impact damage on a stiffened composite panel”. *Composites Part A*. 41(6): 737-749.

Ferrier, E., O. Rabinovitch, and L. Michel. 2016. “Mechanical behavior of concrete-resin/adhesive-FRP structural assemblies under low and high temperatures”. *Construction and Building Materials*. 127: 1017.

Hashin, Z., and A. Rotem. 1973. “Fatigue Failure Criterion for Fibre Reinforced Materials”. *Journal of Composite Materials*. 7: 448-64.

Hashin, Z. 1980. “Failure Criteria for Unidirectional Fibre Composites”. *Journal of Applied Mechanics*, *Transactions ASME*. 47: 329-34.

Imran, M., M. Mahendran, and P. Keerthan. 2018. Experimental and Numerical Studies of CFRP Strengthened Short SHS Steel Columns. Engineering Structures. 175: 879-94.

Imran, M., and M. Mahendran. 2020. “Fire behaviour of CFRP strengthened short SHS steel columns with and without insulation”. *Composites Part B*. 193: 108016.

Imran, M., M. Mahendran, and P. Keerthan. 2018. “Mechanical Properties of Cold-formed Steel Tubular Sections at Elevated Temperatures”. *Journal of Constructional Steel Research*. 143: 131-47.

Imran, M., M. Mahendran, and P. Keerthan. 2018. “Heat Transfer Modelling of CFRP Strengthened and Insulated Steel Tubular Columns”. *Construction and Building Materials*. 184: 278-94.

Kabir, M. H., S. Fawzia, T. H. T. Chan, and M. Badawi. 2016. “Numerical studies on CFRP strengthened steel circular members under marine environment”. *Materials and Structures.* 49(10): 4201-4216.

Kodur, V. K. R., L. A. Bisby, and M. F. Green. 2006. “Experimental evaluation of the fire behaviour of insulated fibre-reinforced-polymer-strengthened reinforced concrete columns”. *Fire Safety Journal*. 41: 547-57.

Kodur, V. K. R., and A. Ahmed A. 2010. “Numerical Model for Tracing the Response of FRP-Strengthened RC Beams Exposed to Fire”. *Journal of Composites for Construction.* 14: 730-42.

Lesani, M., M. R. Bahaari and M. M. Shokrieh. 2013. “Numerical investigation of FRP-strengthened tubular T-joints under axial compressive loads”. *Composite Structures.* 100: 71-78.

Liu, F., B. Wu, and D. Wei. 2009. “Failure modes of reinforced concrete beams strengthened with carbon fibre sheet in fire”. *Fire Safety Journal*. 44: 941-50.

Mostofinejad, D., and N. Moshiri. “Compressive Strength of CFRP Composites Used for Strengthening of RC Columns: Comparative Evaluation of EBR and Grooving Methods”. *Journal of Composites for Construction*. 19(5).

NCC. 2016. National Construction Code (NCC) of Australia, Canberra ACT 2601, Australia.

Nguyen, T-C., Y. Bai, X. L. Zhao, and R. Al-Mahaidi. 2011. “Mechanical characterization of steel/CFRP double strap joints at elevated temperatures”. *Composite Structures*. 93: 1604-12.

Nunes, F., J. R. Correia, and N. Silvestre. 2016. “Structural behavior of hybrid FRP pultruded beams: Experimental, numerical and analytical studies”. *Thin-Walled Structures.* 106: 201-217.

Pister, K. S., and S. B. Dong. 1959. “Elastic bending of layered plates”. *Journal of the Engineering Mechanics Division*. 85(4): 1–10.

Proia, A., and S. Matthys. 2017. “Modelling of the flexural behaviour of FRP strengthened beams at elevated temperatures”. *In Proceedings Int Conf Advanced Composites in Construction (ACIC2017)*. 149-154. Sheffield, UK.

Podolski, D. 2017. *Temperature Distribution in Intumescent Coating Protected Steel Sections*. Master of Philosophy thesis, The University of Manchester, Manchester, UK.

Schafer, B. W., and T. Peköz. 1998. “Computational modeling of cold-formed steel: characterizing geometric imperfections and residual stresses”. *Journal of Constructional Steel Research*. 47: 193-210.

Shaat, A., and A. Fam. 2006. “Axial loading tests on short and long hollow structural steel columns retrofitted using carbon fibre reinforced polymers”. *Canadian Journal of Civil Engineering*. 33: 458-70.

SIMULIA. 2011. ABAQUS analysis and theory manuals. Providence: SIMULIA. The Dassault Systèmes, Realistic Simulation, RI, USA.

Standards Australia. 1998. AS 4100, Steel Structures. Sydney, Australia.

Standards Australia/Standards New Zealand. 2005. AS/NZS 4600 Cold-Formed Steel Structures, Sydney, Australia.

Teng J. G., D. Fernando D., and T. Yu. 2015. Finite element modelling of debonding failures in steel beams flexurally strengthened with CFRP laminates. *Engineering Structures*. 86: 213-24.

Table 1. Ambient temperature mechanical properties of steel

Parameter	Value
Elastic Modulus	207 GPa
Yield strength	359 MPa
Ultimate strength	407 MPa
Poisson's ratio	0.3

Table 2. Ambient temperature material properties of adhesive

Parameter	Value
E_a	1.995 GPa
$\sigma_{\max}$	49.3 MPa
$\tau_{\max}$	44.4 MPa
k_{nn}	1.995×10^{13} N/m^3
$k_{ss} = k_{tt}$	1.0×10^{13} N/m^3
G_I	3900 N/m
G_{II}	11000 N/m

Table 3. Ambient temperature material properties of CFRP

Parameter	Value
E_{1C}	88.6 GPa
E_{2C}	22.2 GPa
T^L	903 MPa
G_{ft}	91600 N/m
G_{fc}	79900 N/m
G_{mt}	220 N/m
G_{mc}	1100 N/m

Table 4. Comparison of experimental and FEA failure loads

Test Column	Failure load (kN)		FEA/Experiment
	Experiment	FEA	
SS -20	281.6	291.3	1.03
SS -66	263.4	274.1	1.04
SS -81	228.1	231.8	1.02
SS -100	197.4	205.4	1.04
SS -150	180.1	188.3	1.05
SS -200	167.5	165.9	0.99
SS -225	164.5	162.6	0.99

Table 5. Elevated temperature axial compression capacities of Grade 450 100×100×2 SHS

CFRP Config.	Temperature (°C)	$P_{u,T}$ (kN)	$P_{u,T}$ $/P_{u,20}$	λ_T	$P_{u,T}/P_{y,T}$	$P_{u,T,th}$ (kN)	$P_{u,T}$ $/P_{u,T,th}$
Bare	20	244.1	1.00	1.136	0.701	254.7	0.96
	100	241.8	0.99	1.137	0.700	252.4	0.96
	150	239.5	0.98	1.137	0.700	250.0	0.96
	200	235.9	0.97	1.136	0.701	246.2	0.96
	225	233.4	0.96	1.136	0.701	243.5	0.96
	300	222.0	0.91	1.132	0.702	231.6	0.96
	400	193.2	0.79	1.121	0.708	201.4	0.96
	500	145.7	0.60	1.090	0.724	149.8	0.97
	600	89.5	0.37	1.042	0.746	91.2	0.98
	700	45.5	0.19	1.002	0.777	45.8	0.99
	800	20.2	0.08	0.937	0.802	20.2	1.00
1T	20	310.8	1.00	0.890	0.893	294.3	1.06
	66	279.7	0.90	0.956	0.803	288.7	0.97
	81	253.6	0.82	1.070	0.731	268.2	0.95
	100	244.0	0.79	1.100	0.707	260.0	0.94
	150	240.1	0.77	1.113	0.702	254.0	0.95
	200	236.1	0.76	1.126	0.701	247.2	0.96
1L	20	343.5	1.00	0.860	0.987	304.9	1.13
	66	283.7	0.83	0.927	0.815	298.5	0.95
	81	259.5	0.76	1.054	0.748	273.3	0.95
	100	250.3	0.73	1.091	0.725	262.8	0.95
	150	241.9	0.70	1.107	0.708	255.5	0.95
	200	236.5	0.69	1.125	0.703	247.6	0.96
1T1L	20	412.3	1.00	0.616	1.184	354.7	1.16
	66	325.7	0.79	0.739	0.935	350.1	0.93
	81	290.1	0.70	0.931	0.836	313.8	0.92
	100	272.8	0.66	1.013	0.790	288.6	0.95
	150	255.9	0.62	1.056	0.748	270.8	0.94
	200	236.9	0.57	1.112	0.704	252.1	0.94

Table 6. Elevated temperature axial compression capacities of Grade 450 200×200×2 SHS

CFRP Config.	Temperature (°C)	$P_{u,T}$ (kN)	$P_{u,T}$ $/P_{u,20}$	λ_T	$P_{u,T}/P_{y,T}$	$P_{u,T,th}$ (kN)	$P_{u,T}$ $/P_{u,T,th}$
Bare	20	275.2	1.00	2.215	0.389	284.9	0.97
	100	273.9	1.00	2.216	0.390	282.4	0.97
	150	272.1	0.99	2.216	0.391	279.7	0.97
	200	269.3	0.98	2.215	0.393	275.4	0.98
	225	265.7	0.97	2.214	0.392	272.5	0.98
	300	253.5	0.92	2.207	0.394	259.2	0.98
	400	220.3	0.80	2.185	0.397	225.8	0.98
	500	166.7	0.61	2.125	0.407	168.5	0.99
	600	102.9	0.37	2.030	0.422	103.2	1.00
	700	52.5	0.19	1.921	0.441	52.3	1.00
	800	23.9	0.09	1.824	0.467	23.3	1.03
1T	20	370.6	1.00	1.714	0.523	340.8	1.09
	66	329.0	0.89	1.828	0.465	329.4	1.00
	81	292.1	0.79	2.075	0.414	303.7	0.96
	100	278.5	0.75	2.142	0.397	292.7	0.95
	150	269.8	0.73	2.169	0.388	285.1	0.95
	200	267.2	0.72	2.197	0.390	276.8	0.97
1L	20	410.3	1.00	1.673	0.579	356.9	1.15
	66	337.7	0.82	1.792	0.477	347.6	0.97
	81	308.7	0.75	2.055	0.438	310.8	0.99
	100	296.1	0.72	2.131	0.422	296.4	1.00
	150	278.3	0.68	2.161	0.400	287.1	0.97
	200	267.5	0.65	2.195	0.391	277.3	0.96
1T1L	20	565.5	1.00	1.155	0.799	445.0	1.27
	66	402.7	0.71	1.321	0.569	436.8	0.92
	81	358.0	0.63	1.766	0.507	371.8	0.96
	100	326.6	0.58	1.964	0.465	333.1	0.98
	150	300.6	0.53	2.055	0.432	308.3	0.97
	200	275.8	0.49	2.172	0.403	283.4	0.97
2T2L	20	786.0	1.00	0.664	1.110	609.5	1.29
	66	586.5	0.75	0.828	0.828	610.8	0.96
	81	472.5	0.60	1.228	0.670	544.1	0.87
	100	408.0	0.52	1.515	0.581	466.5	0.87
	150	361.5	0.46	1.710	0.520	400.7	0.90
	200	283.4	0.36	2.062	0.414	316.2	0.90

Table 7. Elevated temperature axial compression capacities of Grade 450 200×200×5 SHS

CFRP Config.	Temperature (°C)	$P_{u,T}$ (kN)	$P_{u,T}$ $/P_{u,20}$	λ_T	$P_{u,T}/P_{y,T}$	$P_{u,T,th}$ (kN)	$P_{u,T}$ $/P_{u,T,th}$
Bare	20	1407.0	1.00	0.897	0.820	1513.0	0.93
	100	1392.9	0.99	0.898	0.818	1499.7	0.93
	150	1380.3	0.98	0.898	0.819	1485.1	0.93
	200	1359.0	0.97	0.897	0.819	1462.3	0.93
	225	1343.8	0.96	0.897	0.819	1446.7	0.93
	300	1277.6	0.91	0.894	0.820	1375.3	0.93
	400	1110.0	0.79	0.885	0.825	1194.7	0.93
	500	832.0	0.59	0.861	0.838	895.9	0.93
	600	507.0	0.36	0.822	0.857	547.8	0.93
	700	253.7	0.18	0.778	0.878	275.6	0.92
	800	111.4	0.08	0.739	0.897	121.7	0.92
1T	20	1572.2	1.00	0.836	0.916	1557.4	1.01
	66	1471.5	0.94	0.856	0.857	1538.9	0.96
	81	1418.8	0.90	0.887	0.829	1515.8	0.94
	100	1403.1	0.89	0.892	0.824	1505.4	0.93
	150	1386.2	0.88	0.894	0.822	1488.0	0.93
	200	1360.5	0.87	0.897	0.820	1463.1	0.93
1L	20	1619.7	1.00	0.818	0.944	1584.0	1.02
	66	1454.0	0.90	0.842	0.847	1564.0	0.93
	81	1437.1	0.89	0.883	0.840	1523.2	0.94
	100	1416.9	0.87	0.890	0.832	1508.9	0.94
	150	1393.1	0.86	0.893	0.827	1489.8	0.94
	200	1361.5	0.84	0.896	0.820	1463.5	0.93
1T1L	20	1734.3	1.00	0.732	1.010	1671.0	1.04
	66	1542.9	0.89	0.781	0.899	1644.3	0.94
	81	1479.7	0.85	0.859	0.865	1560.5	0.95
	100	1441.0	0.83	0.878	0.847	1527.9	0.94
	150	1407.9	0.81	0.886	0.835	1499.9	0.94
	200	1365.0	0.79	0.895	0.823	1466.2	0.93
2T2L	20	2085.0	1.00	0.572	1.215	1857.0	1.12
	66	1784.8	0.86	0.673	1.040	1834.9	0.97
	81	1590.0	0.76	0.790	0.930	1699.7	0.94
	100	1522.0	0.73	0.838	0.894	1612.2	0.94
	150	1457.6	0.70	0.861	0.865	1548.6	0.94
	200	1376.3	0.66	0.889	0.829	1479.9	0.93

Table 8. Elevated temperature axial compression capacities of Grade 450 350×350×8 SHS

CFRP Config.	Temperature (°C)	$P_{u,T}$ (kN)	$P_{u,T}/P_{u,20}$	λ_T	$P_{u,T}/P_{y,T}$	$P_{u,T,th}$ (kN)	$P_{u,T}/P_{u,T,th}$
Bare	20	3680.0	1.00	0.986	0.763	3991.4	0.92
	100	3651.8	0.99	0.986	0.763	3956.5	0.92
	150	3619.2	0.98	0.986	0.764	3917.8	0.92
	200	3568.4	0.97	0.986	0.765	3857.8	0.92
	225	3528.6	0.96	0.985	0.765	3816.7	0.92
	300	3360.0	0.91	0.982	0.767	3628.7	0.93
	400	2932.8	0.80	0.973	0.776	3153.7	0.93
	500	2184.0	0.59	0.945	0.782	2361.6	0.92
	600	1336.2	0.36	0.904	0.803	1443.8	0.93
	700	672.4	0.18	0.855	0.828	727.1	0.92
	800	297.3	0.08	0.812	0.852	321.6	0.92
1T	20	3872.6	1.00	0.947	0.802	4047.4	0.96
	66	3785.6	0.98	0.961	0.784	4013.6	0.94
	81	3692.0	0.95	0.981	0.768	3980.9	0.93
	100	3668.0	0.95	0.983	0.766	3962.8	0.93
	150	3628.0	0.94	0.984	0.766	3921.1	0.93
	200	3570.5	0.92	0.985	0.765	3858.7	0.93
1L	20	3966.3	1.00	0.934	0.822	4097.3	0.97
	66	3758.0	0.95	0.951	0.779	4056.7	0.93
	81	3725.6	0.94	0.978	0.775	3992.5	0.93
	100	3689.2	0.93	0.982	0.771	3968.2	0.93
	150	3638.7	0.92	0.984	0.768	3923.8	0.93
	200	3569.1	0.90	0.985	0.765	3859.4	0.92
1T1L	20	4210.4	1.00	0.880	0.872	4222.4	1.00
	66	3904.1	0.93	0.913	0.809	4164.8	0.94
	81	3776.0	0.90	0.965	0.785	4034.1	0.94
	100	3717.6	0.88	0.976	0.777	3988.3	0.93
	150	3656.8	0.87	0.980	0.772	3934.3	0.93
	200	3600.0	0.86	0.985	0.772	3862.1	0.93
2T2L	20	4870.0	1.00	0.756	1.009	4605.2	1.06
	66	4240.0	0.87	0.818	0.879	4523.0	0.94
	81	3960.0	0.81	0.922	0.824	4212.4	0.94
	100	3820.0	0.78	0.956	0.798	4081.7	0.94
	150	3714.5	0.76	0.969	0.784	3984.6	0.93
	200	3584.2	0.74	0.982	0.768	3875.4	0.92

Table 9. Critical temperatures of Grade 450 100×100×2 SHS

Load ratio	Bare	1T	1L	1T1L
0.1	782	753	738	713
0.2	691	658	643	614
0.3	633	593	575	539
0.4	584	538	515	463
0.5	542	481	449	361
0.6	498	417	361	172
0.7	451	319	162	82
0.8	394	87	72	64
0.9	310	66	47	42
1	20	20	20	20

Table 10. Critical temperatures of Grade 450 200×200×2 SHS

Load ratio	Bare	1T	1L	1T1L	2T2L
0.1	786	749	734	690	644
0.2	693	653	637	583	515
0.3	637	586	567	495	359
0.4	588	529	504	386	180
0.5	545	468	432	185	113
0.6	503	393	326	89	81
0.7	455	271	123	68	72
0.8	393	79	71	57	52
0.9	311	62	46	36	38
1	20	20	20	20	20

Table 11. Critical temperatures of Grade 450 200×200×5 SHS

Load ratio	Bare	1T	1L	1T1L	2T2L
0.1	778	765	761	752	726
0.2	687	672	668	659	632
0.3	630	613	607	595	563
0.4	582	562	556	542	499
0.5	540	515	507	488	428
0.6	496	463	453	428	319
0.7	449	404	389	344	149
0.8	393	315	285	175	75
0.9	311	83	65	62	53
1	20	20	20	20	20

Table 12. Critical temperatures of Grade 450 350×350×8 SHS

Load ratio	Bare	1T	1L	1T1L	2T2L
0.1	780	774	771	764	744
0.2	688	681	678	670	650
0.3	631	623	619	609	584
0.4	583	573	569	558	528
0.5	540	529	524	510	469
0.6	497	483	476	457	402
0.7	451	433	424	398	284
0.8	398	368	351	297	86
0.9	314	248	199	79	56
1	20	20	20	20	20

(a) (b)

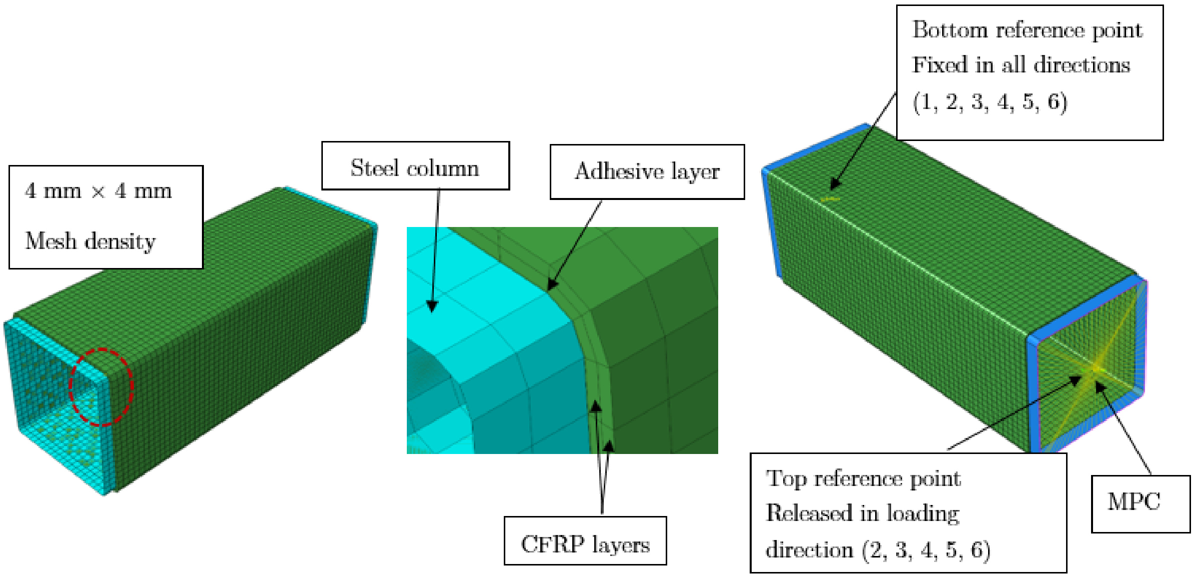
4 mm × 4 mm
Mesh density
Steel column
Adhesive layer
CFRP layers
Bottom reference point
Fixed in all directions
(1, 2, 3, 4, 5, 6)
Top reference point
Released in loading
direction (2, 3, 4, 5, 6)
MPC

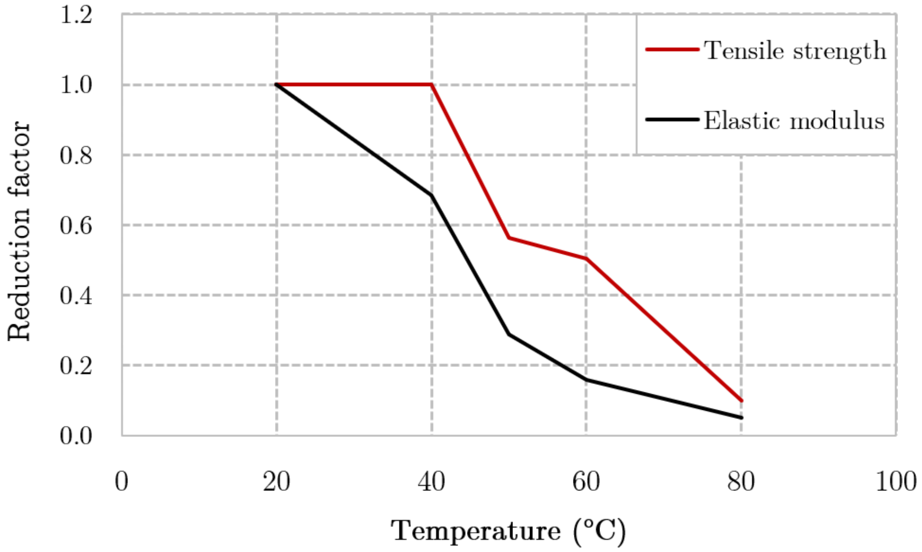

1.2
1.0
0.8
0.6
0.4
0.2
0.0
Reduction factor
0
20
40
60
80
100
Temperature (°C)
Tensile strength
Elastic modulus

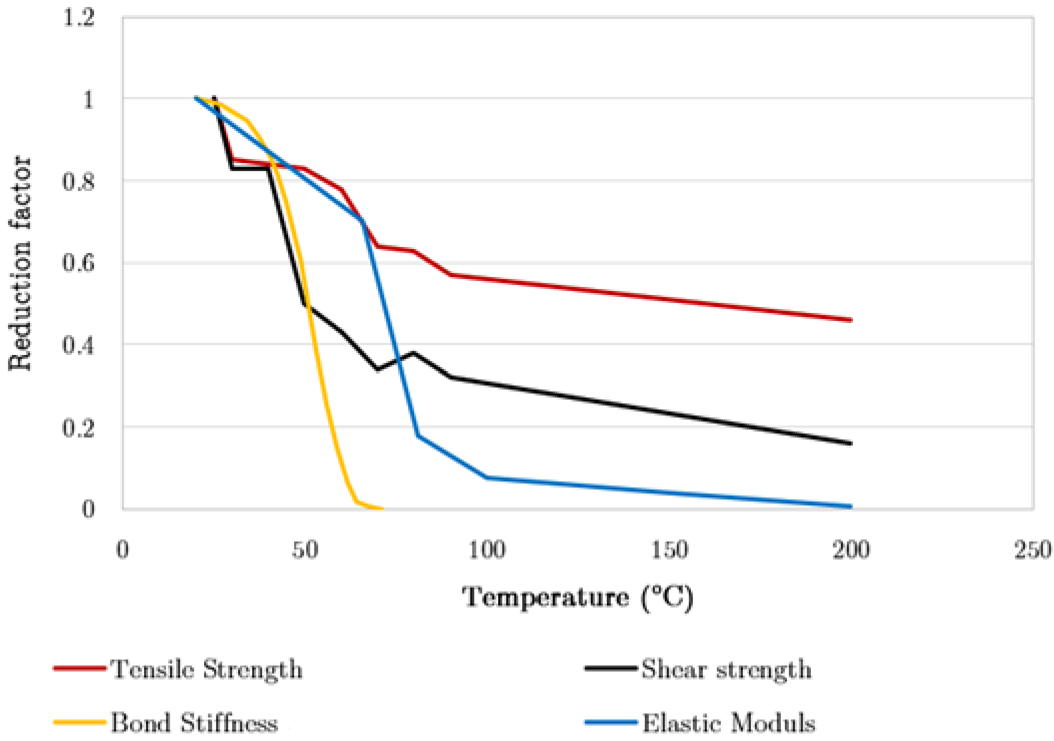

1.2
1
0.8
0.6
0.4
0.2
0
Reduction factor
0
50
100
150
200
250
Temperature (°C)
Tensile Strength
Shear strength
Bond Stiffness
Elastic Moduls

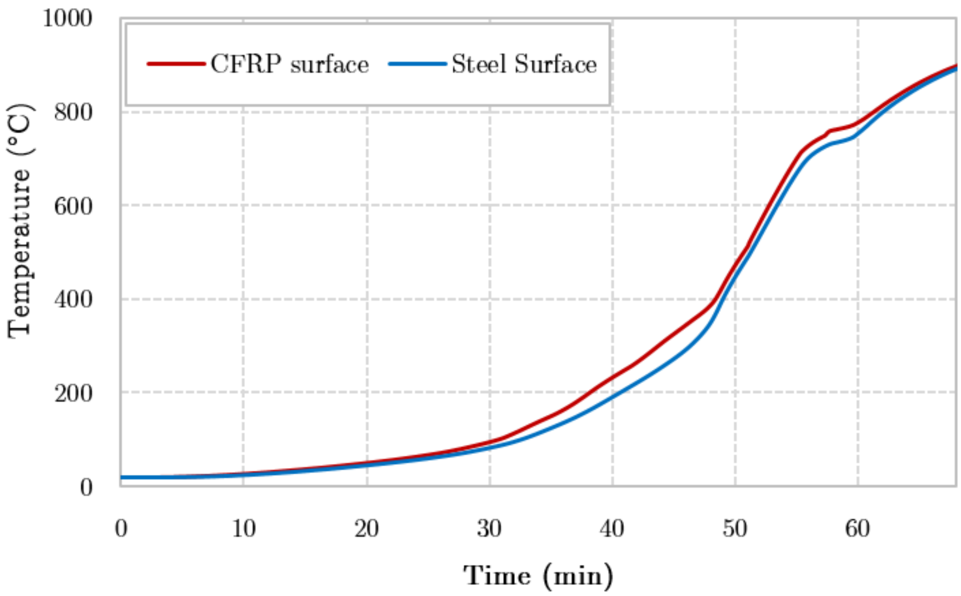
CFRP surface
Steel Surface
Temperature (°C)
Time (min)
1000
800
600
400
200
0
0
10
20
30
40
50
60

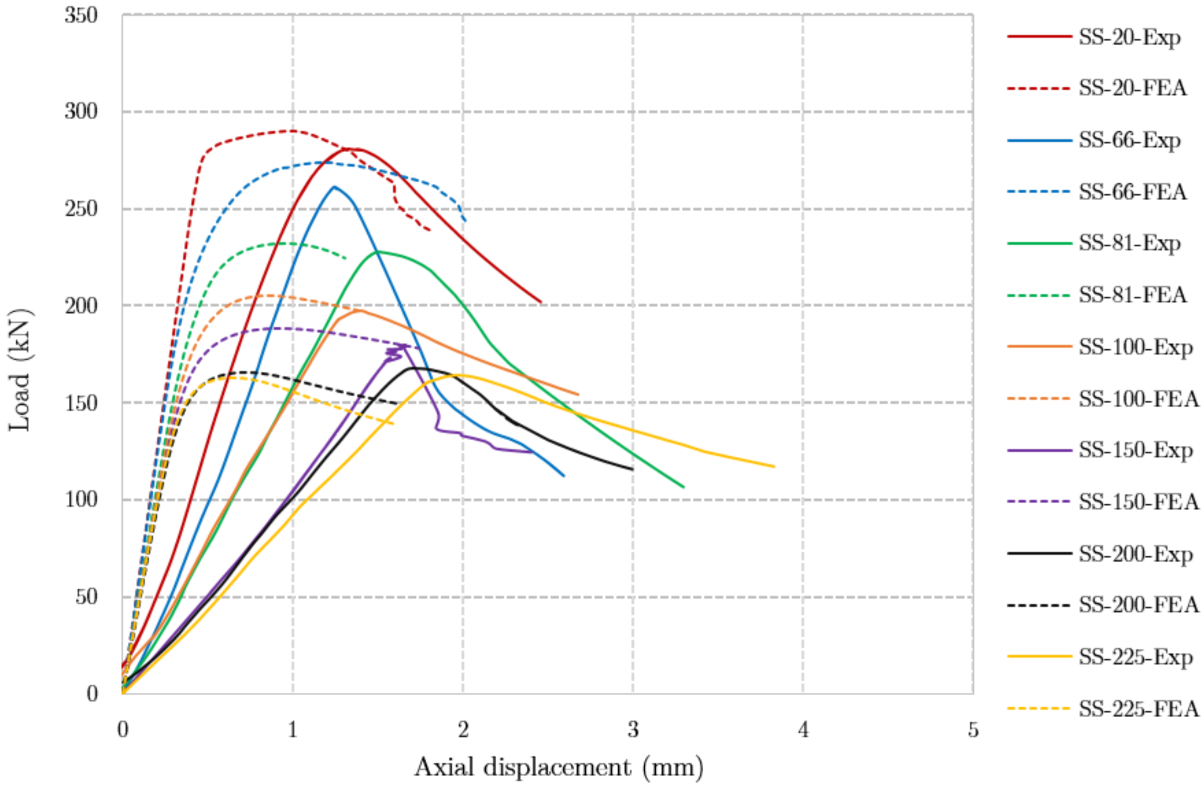

350
300
250
200
150
100
50
0
Load (kN)
0
1
2
3
4
5
Axial displacement (mm)
SS-20-Exp
SS-20-FEA
SS-66-Exp
SS-66-FEA
SS-81-Exp
SS-81-FEA
SS-100-Exp
SS-100-FEA
SS-150-Exp
SS-150-FEA
SS-200-Exp
SS-200-FEA
SS-225-Exp
SS-225-FEA

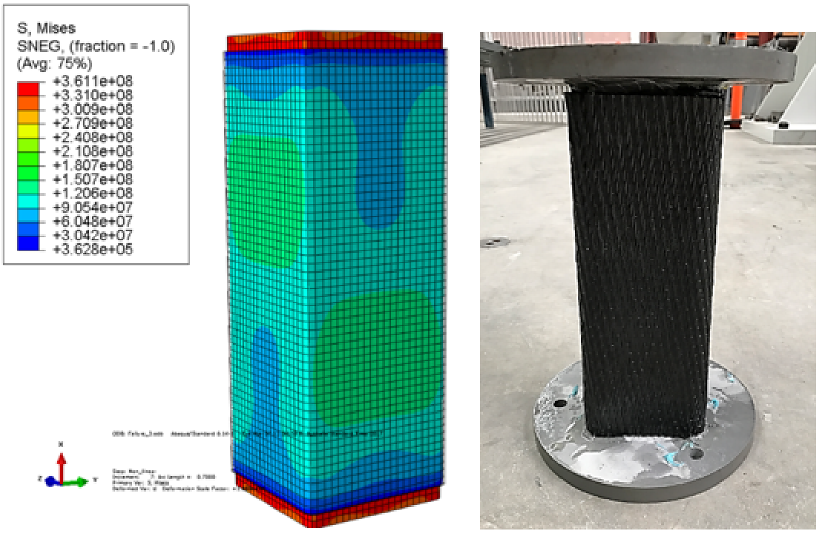
S, Mises
SNEG, (fraction = -1.0)
(Avg: 75%)
+3.611e+08
+3.310e+08
+3.009e+08
+2.709e+08
+2.408e+08
+2.108e+08
+1.807e+08
+1.507e+08
+1.206e+08
+9.054e+07
+6.048e+07
+3.042e+07
+3.628e+05

(a)

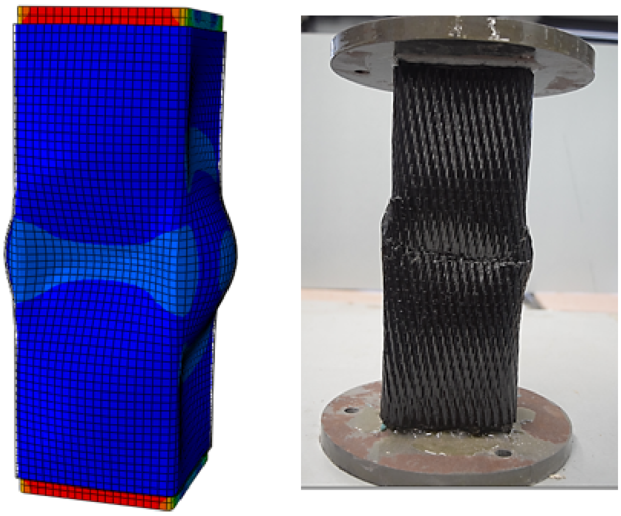

(b)

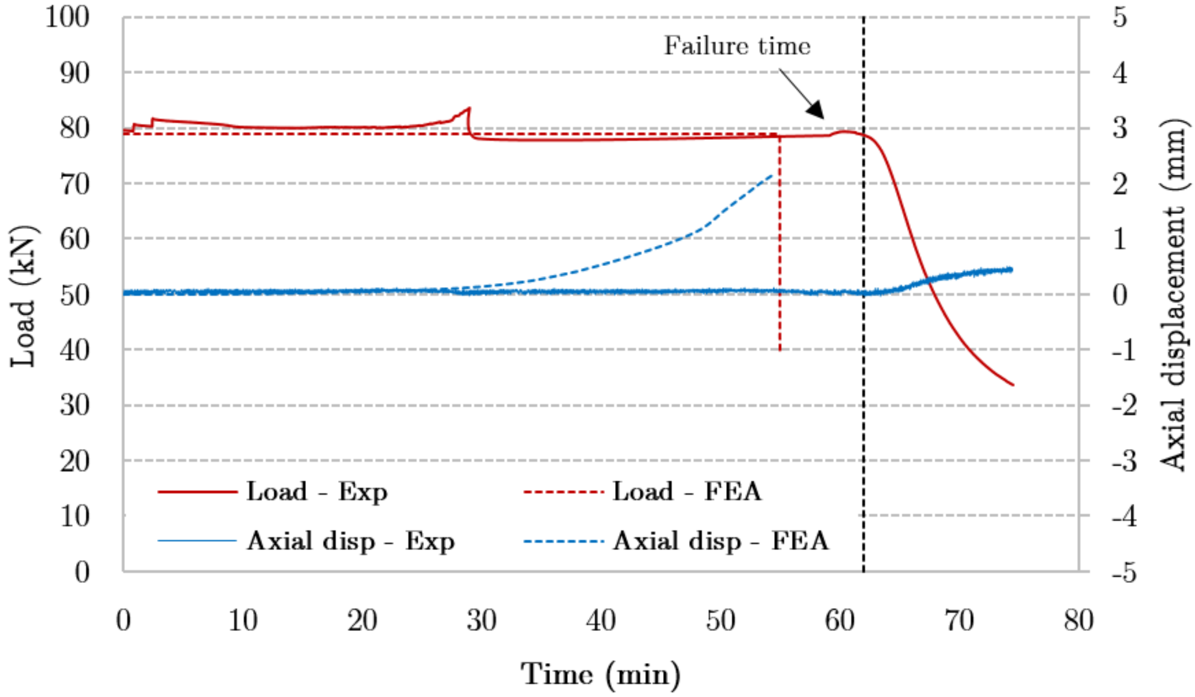

Failure time
Load (kN)
Axial displacement (mm)
Time (min)
Load - Exp
Load - FEA
Axial disp - Exp
Axial disp - FEA
100
90
80
70
60
50
40
30
20
10
0
5
4
3
2
1
0
-1
-2
-3
-4
-5
0
10
20
30
40
50
60
70
80

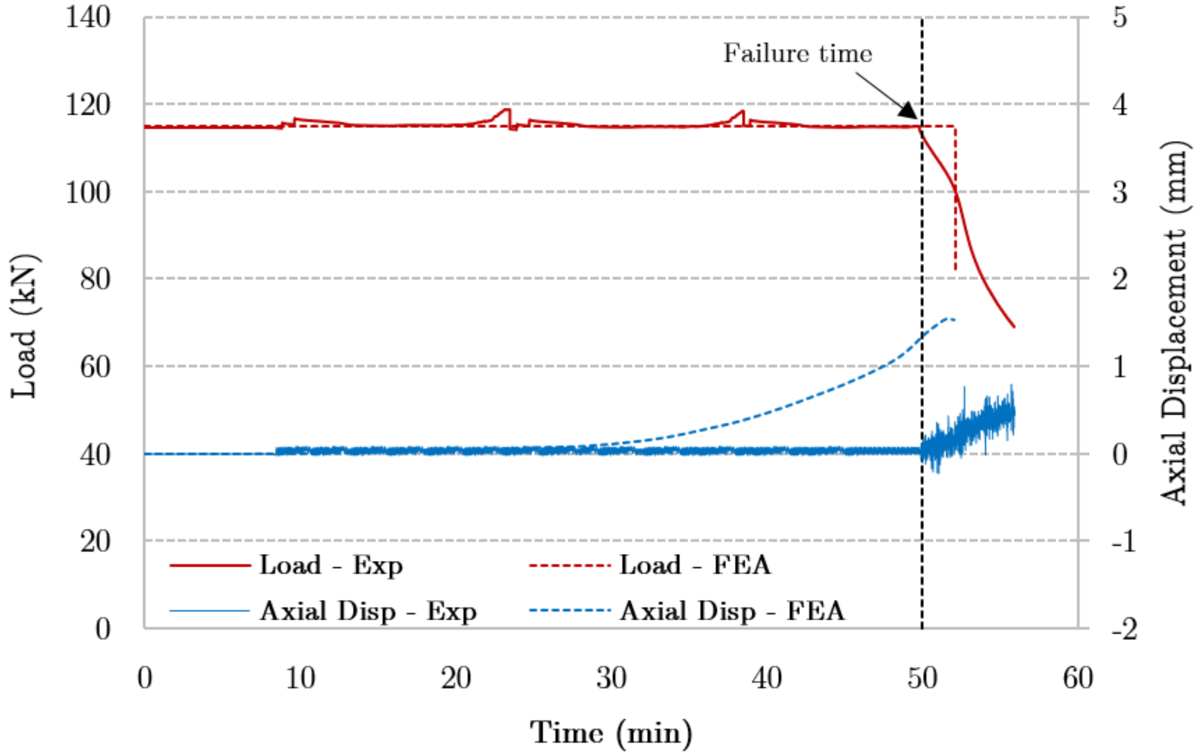

140
120
100
80
60
40
20
0
5
4
3
2
1
0
-1
-2
Load (kN)
Axial Displacement (mm)
Failure time
Load - Exp
Load - FEA
Axial Disp - Exp
Axial Disp - FEA
0
10
20
30
40
50
60
Time (min)

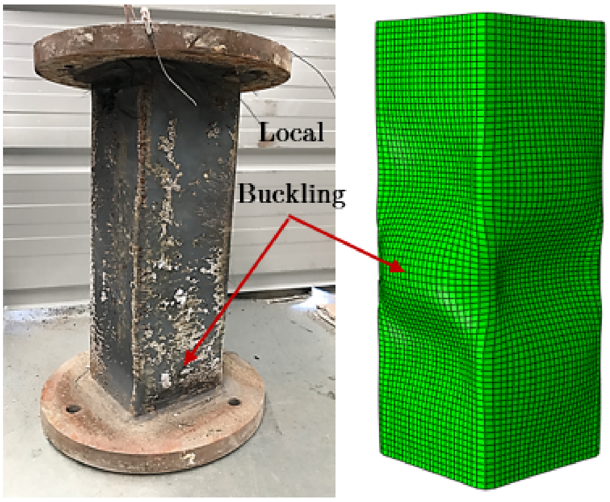

(a)

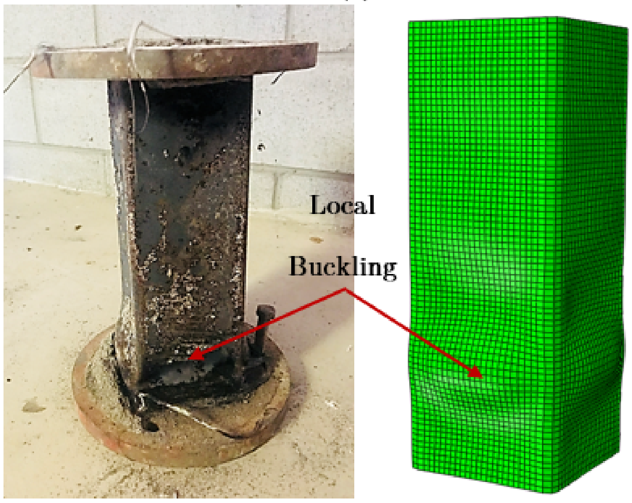

(b)

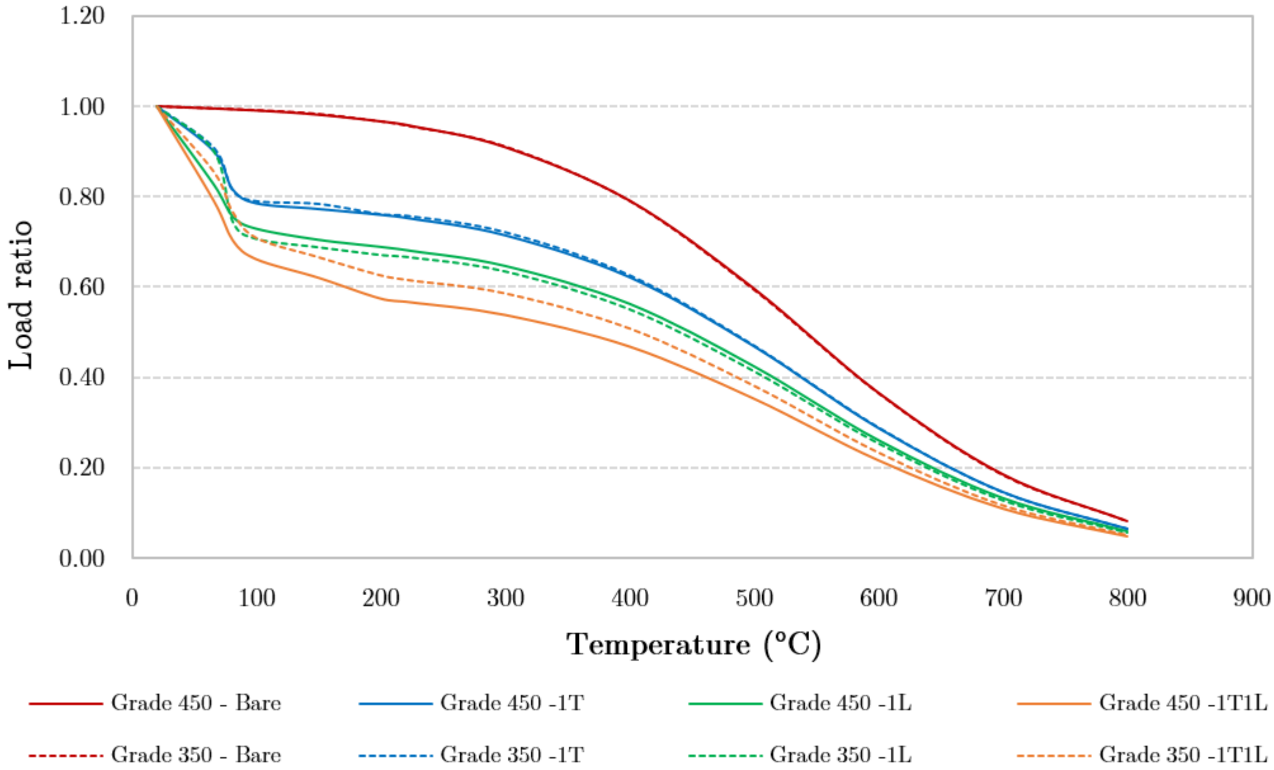

1.20
1.00
0.80
0.60
0.40
0.20
0.00
Load ratio
0
100
200
300
400
500
600
700
800
900
Temperature (°C)
Grade 450 - Bare
Grade 450 -1T
Grade 450 -1L
Grade 450 -1T1L
Grade 350 - Bare
Grade 350 -1T
Grade 350 -1L
Grade 350 -1T1L

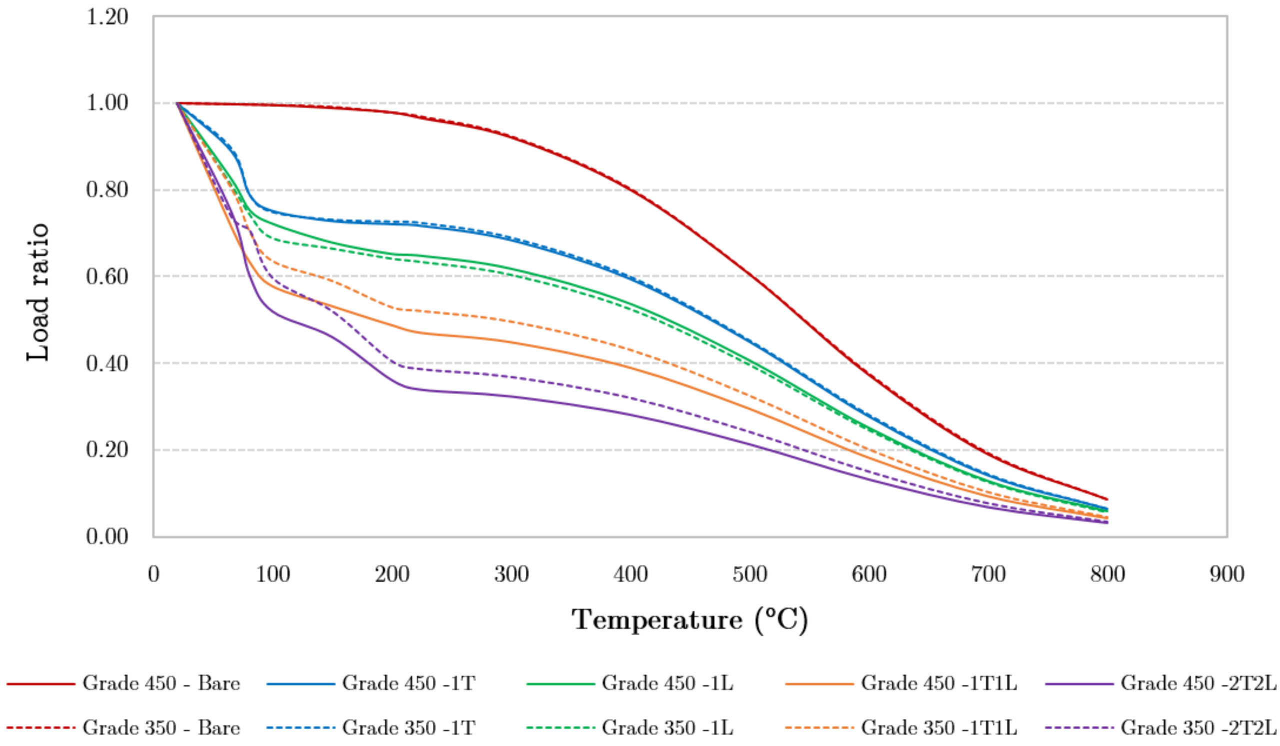
1.20
1.00
0.80
0.60
0.40
0.20
0.00
Load ratio
0
100
200
300
400
500
600
700
800
900
Temperature (°C)
Grade 450 - Bare
Grade 450 -1T
Grade 450 -1L
Grade 450 -1T1L
Grade 450 -2T2L
Grade 350 - Bare
Grade 350 -1T
Grade 350 -1L
Grade 350 -1T1L
Grade 350 -2T2L

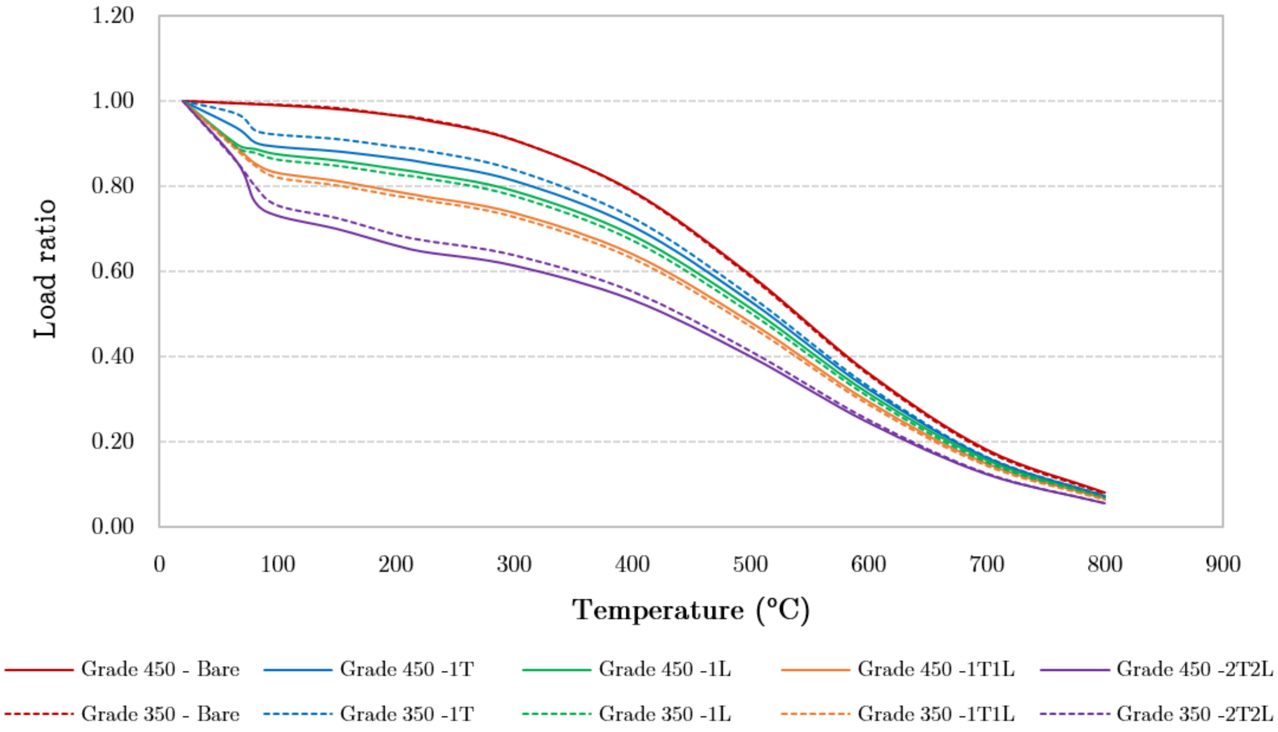
1.20
1.00
0.80
0.60
0.40
0.20
0.00
Load ratio
0
100
200
300
400
500
600
700
800
900
Temperature (°C)
Grade 450 - Bare
Grade 450 -1T
Grade 450 -1L
Grade 450 -1T1L
Grade 450 -2T2L
Grade 350 - Bare
Grade 350 -1T
Grade 350 -1L
Grade 350 -1T1L
Grade 350 -2T2L

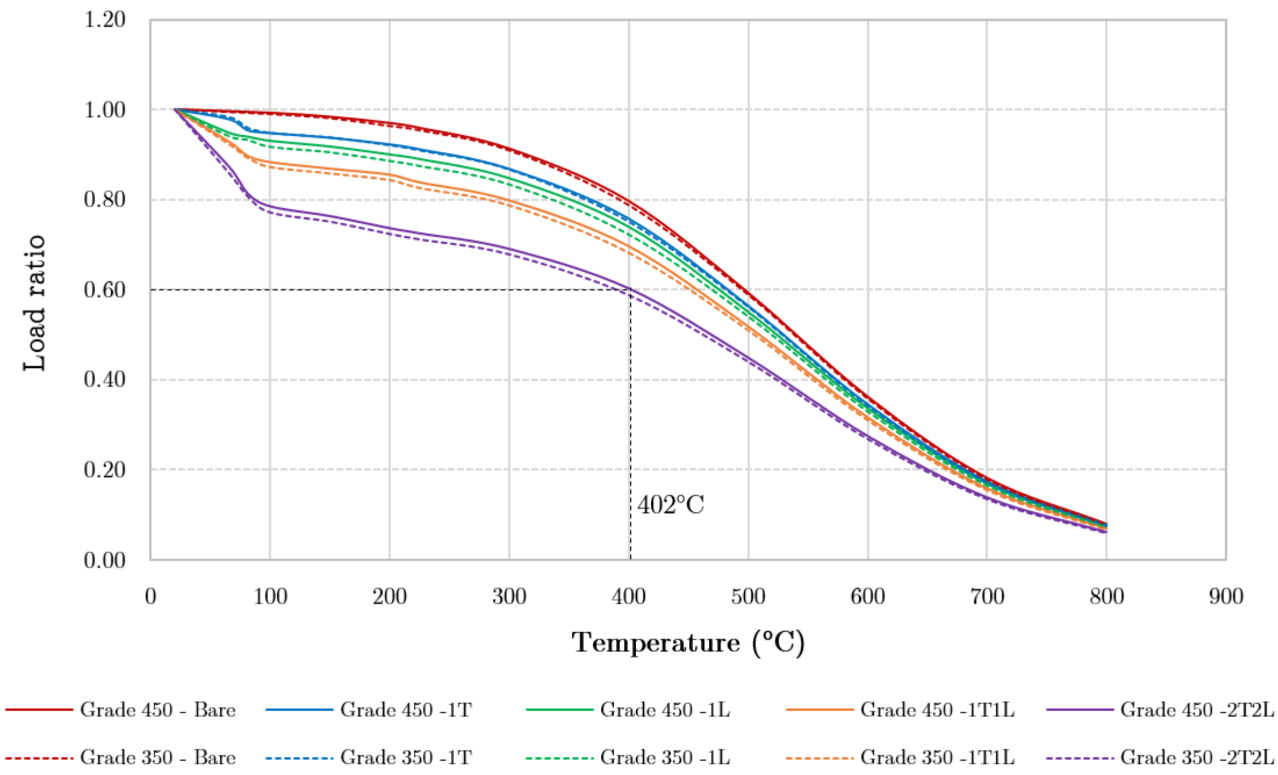

1.20
1.00
0.80
0.60
0.40
0.20
0.00
Load ratio
0
100
200
300
400
500
600
700
800
900
Temperature (°C)
402°C
Grade 450 - Bare
Grade 450 -1T
Grade 450 -1L
Grade 450 -1T1L
Grade 450 -2T2L
Grade 350 - Bare
Grade 350 -1T
Grade 350 -1L
Grade 350 -1T1L
Grade 350 -2T2L

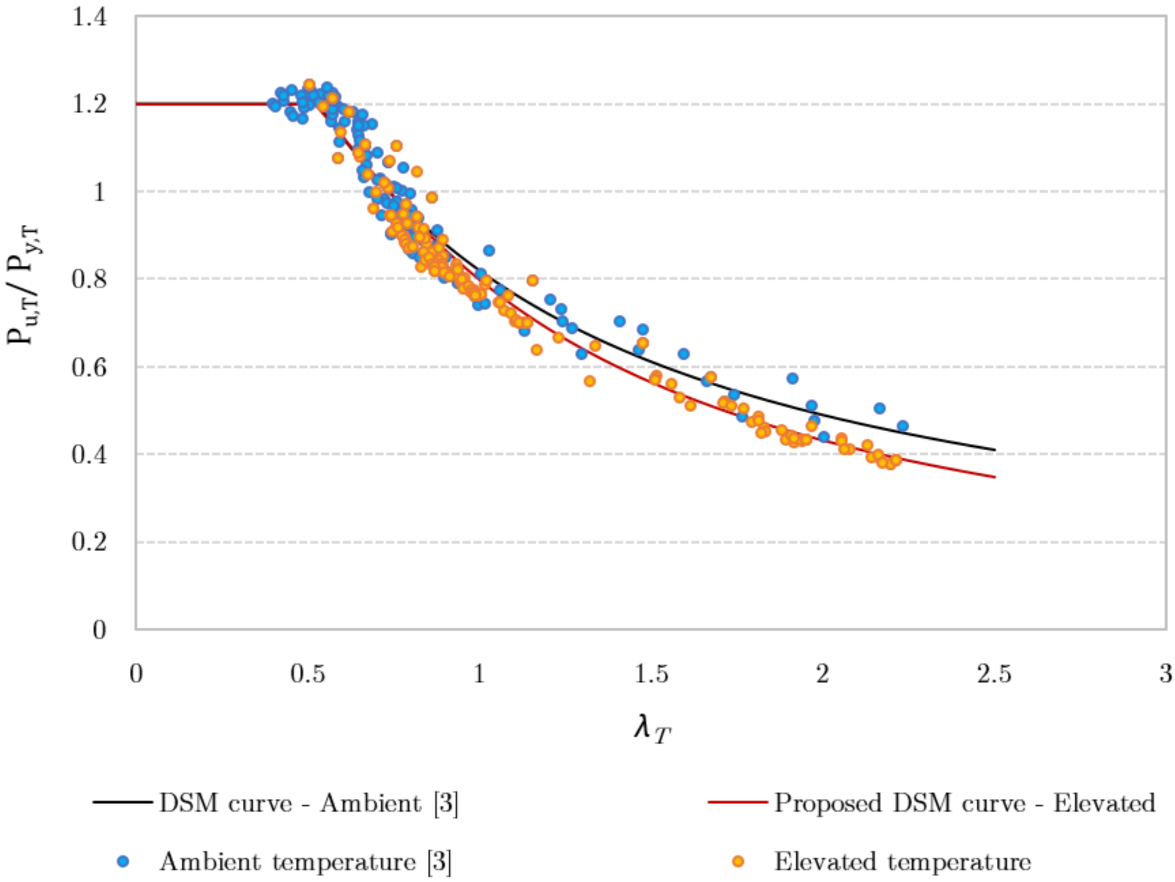

1.4
1.2
1
0.8
0.6
0.4
0.2
0
0
0.5
1
1.5
2
2.5
3
P u,T / P y,T
λ T
DSM curve - Ambient [3]
Proposed DSM curve - Elevated
Ambient temperature [3]
Elevated temperature

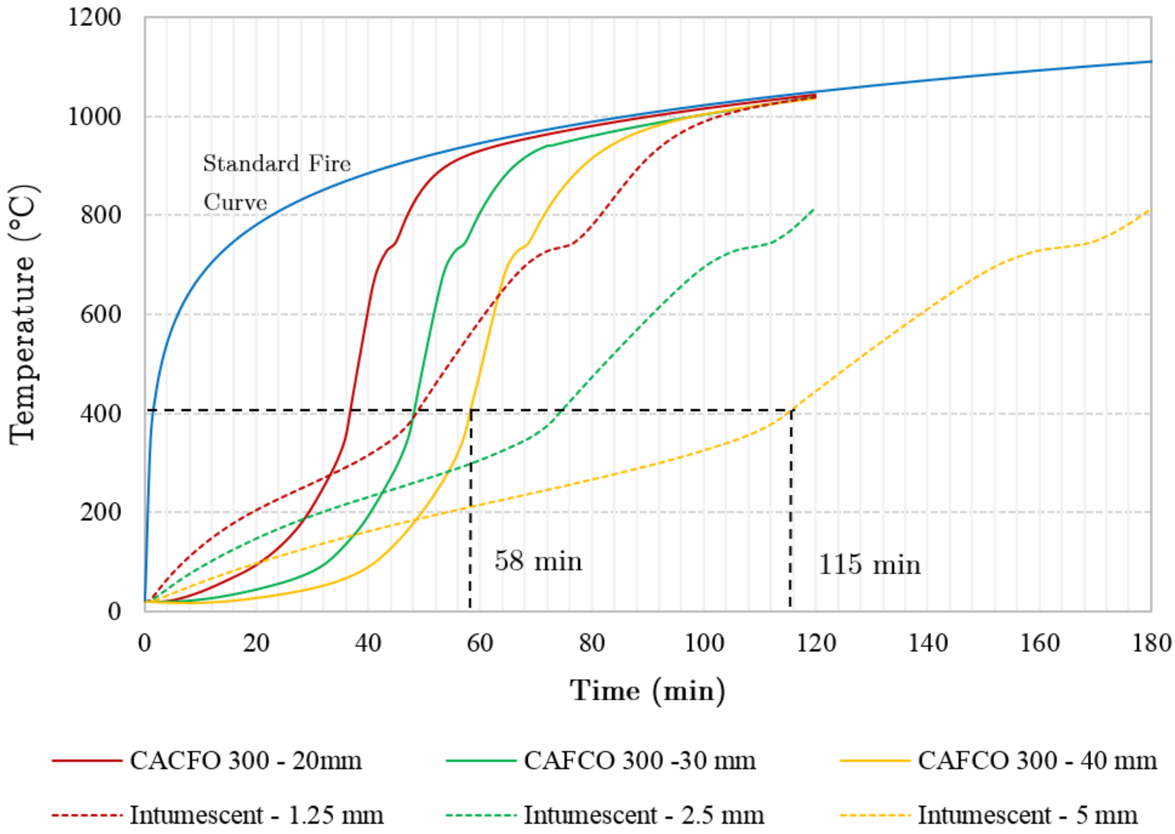

Standard Fire
Curve
58 min
115 min
Temperature (°C)
Time (min)
0
200
400
600
800
1000
1200
0
20
40
60
80
100
120
140
160
180
CACFO 300 - 20mm
CAFCO 300 -30 mm
CAFCO 300 - 40 mm
Intumescent - 1.25 mm
Intumescent - 2.5 mm
Intumescent - 5 mm

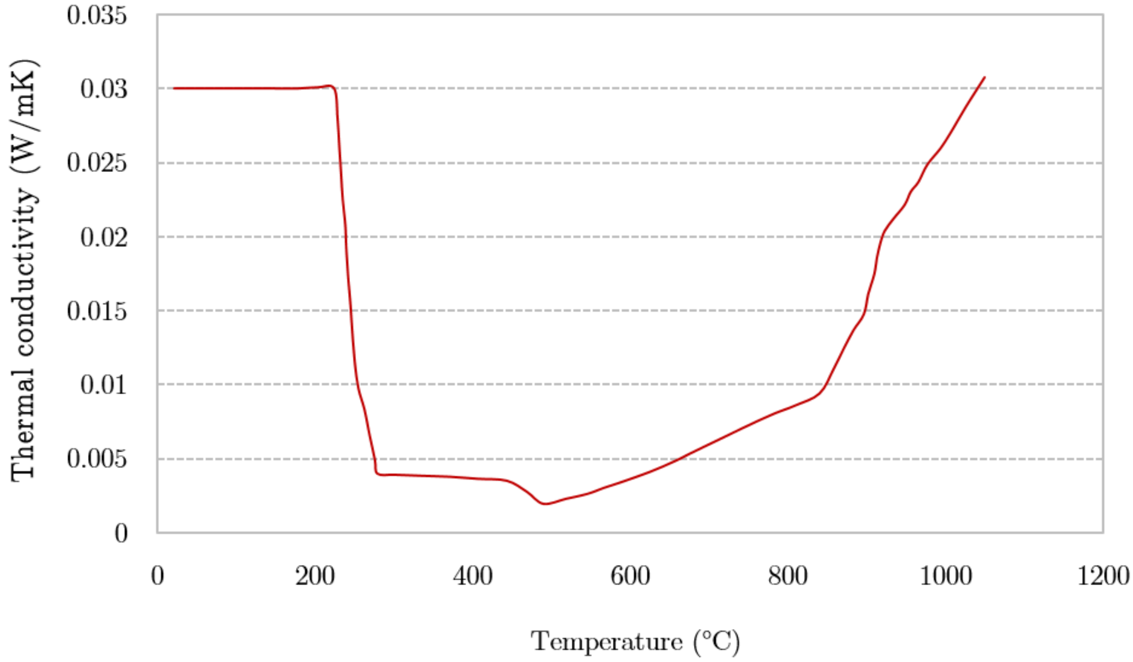

0.035
0.03
0.025
0.02
0.015
0.01
0.005
0
Thermal conductivity (W/mK)
0
200
400
600
800
1000
1200
Temperature (°C)

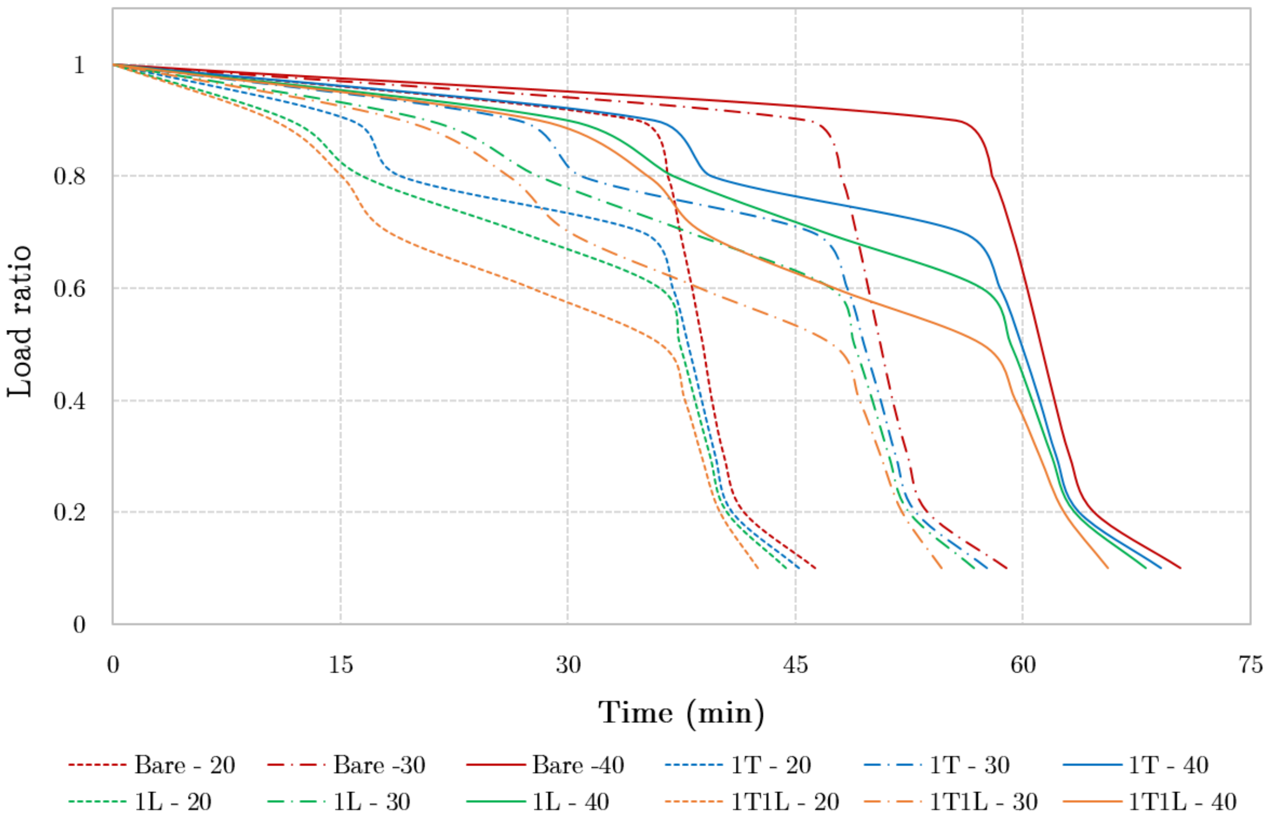
Load ratio
1
0.8
0.6
0.4
0.2
0
0
15
30
45
60
75
Time (min)
Bare - 20
Bare -30
Bare -40
1T - 20
1T - 30
1T - 40
1L - 20
1L - 30
1L - 40
1T1L - 20
1T1L - 30
1T1L - 40

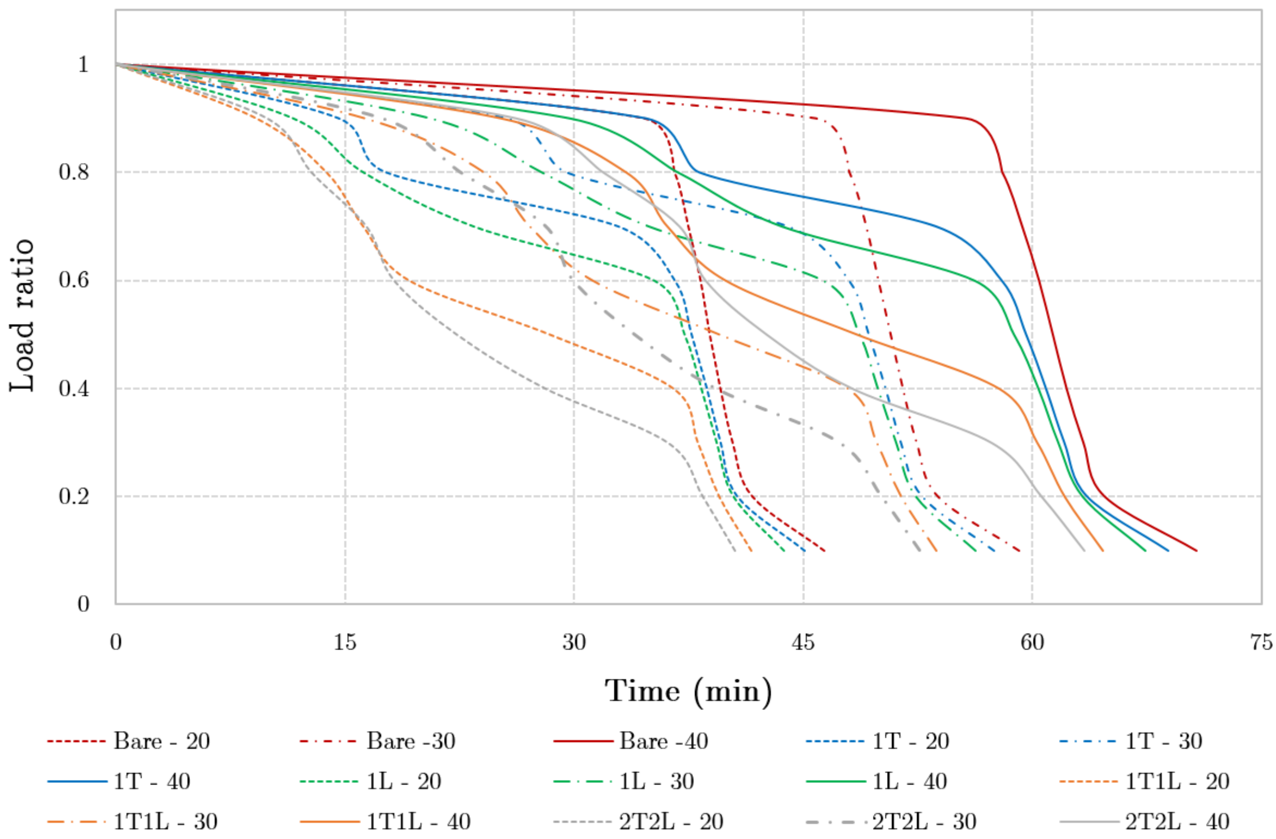

Load ratio
Time (min)
0
0.2
0.4
0.6
0.8
1
0
15
30
45
60
75
Bare - 20
Bare -30
Bare -40
1T - 20
1T - 30
1T - 40
1L - 20
1L - 30
1L - 40
1T1L - 20
1T1L - 30
1T1L - 40
2T2L - 20
2T2L - 30
2T2L - 40

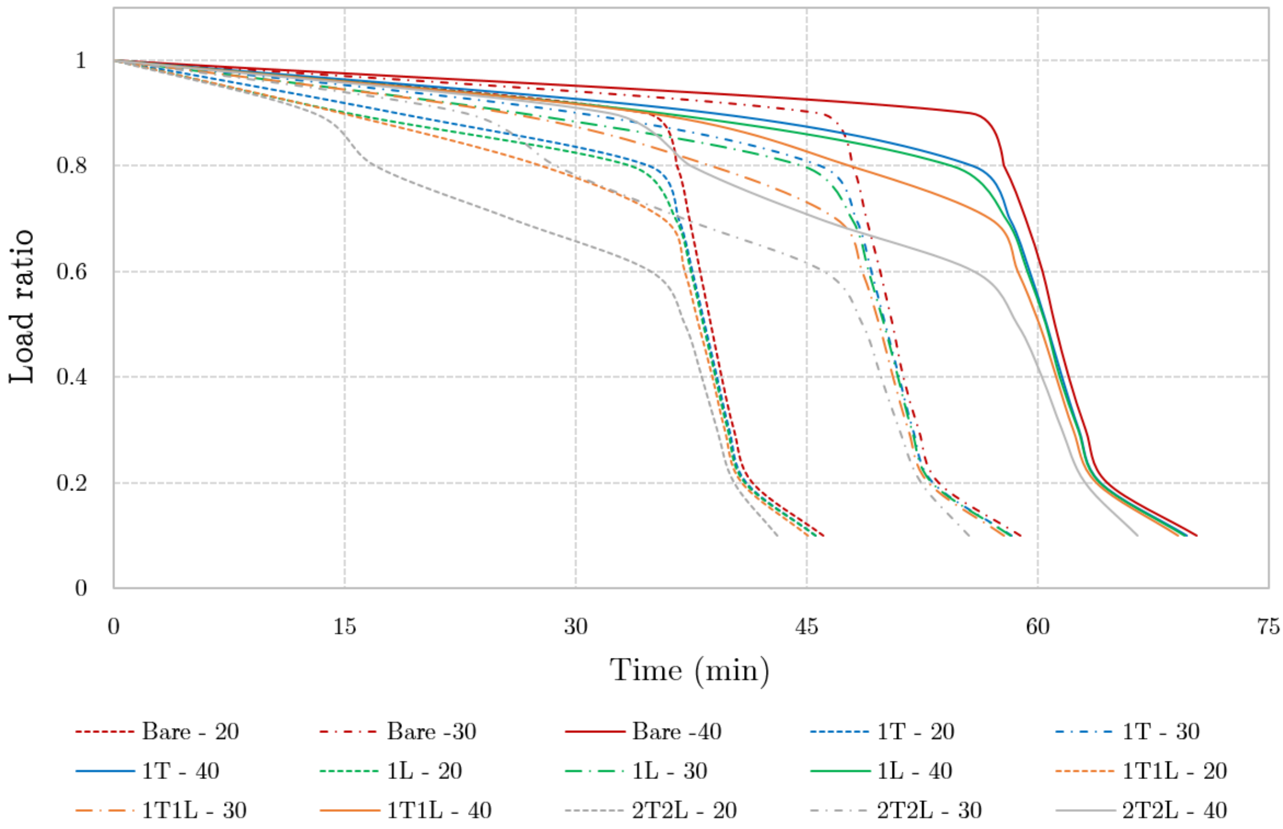

Load ratio
Time (min)
0
0.2
0.4
0.6
0.8
1
0
15
30
45
60
75
Bare - 20
Bare -30
Bare -40
1T - 20
1T - 30
1T - 40
1L - 20
1L - 30
1L - 40
1T1L - 20
1T1L - 30
1T1L - 40
2T2L - 20
2T2L - 30
2T2L - 40

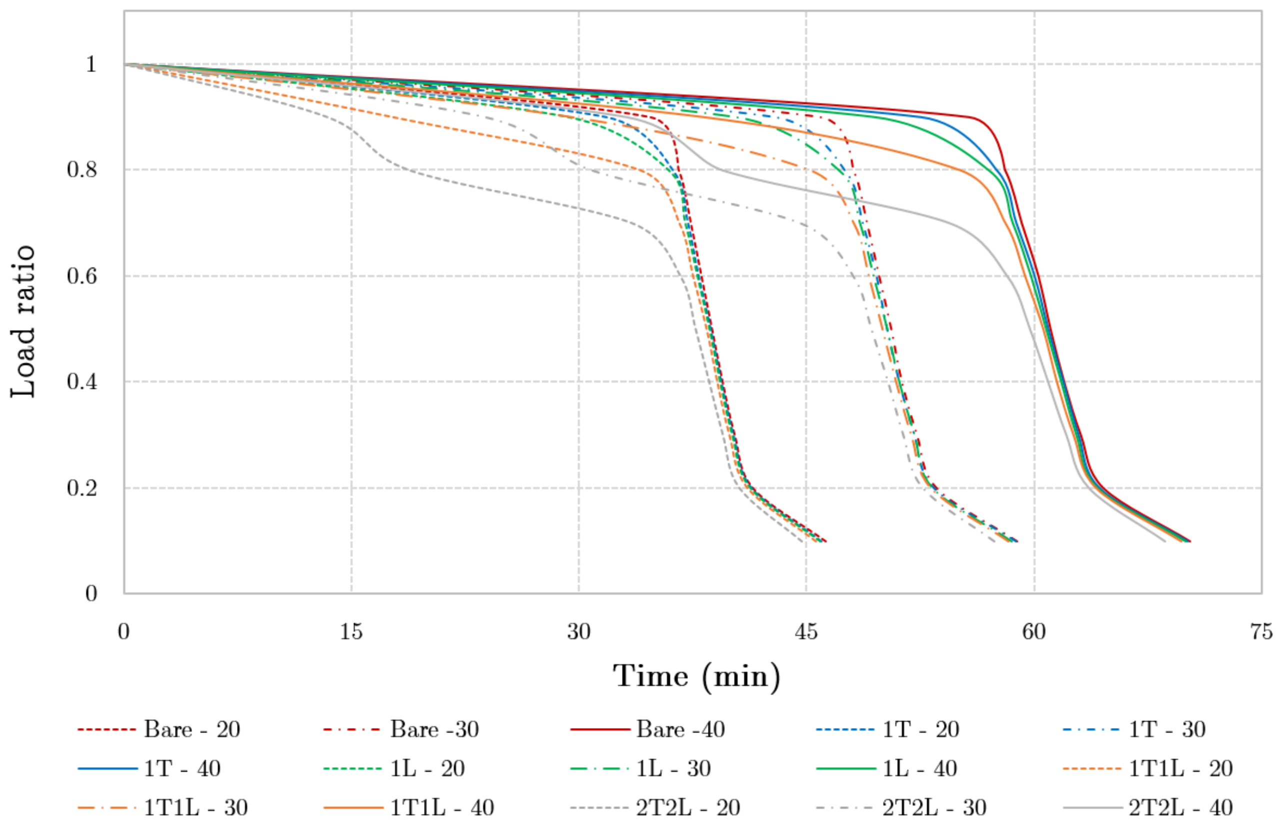
Load ratio
Time (min)
0
0.2
0.4
0.6
0.8
1
0
15
30
45
60
75
Bare - 20
Bare -30
Bare -40
1T - 20
1T - 30
1T - 40
1L - 20
1L - 30
1L - 40
1T1L - 20
1T1L - 30
1T1L - 40
2T2L - 20
2T2L - 30
2T2L - 40

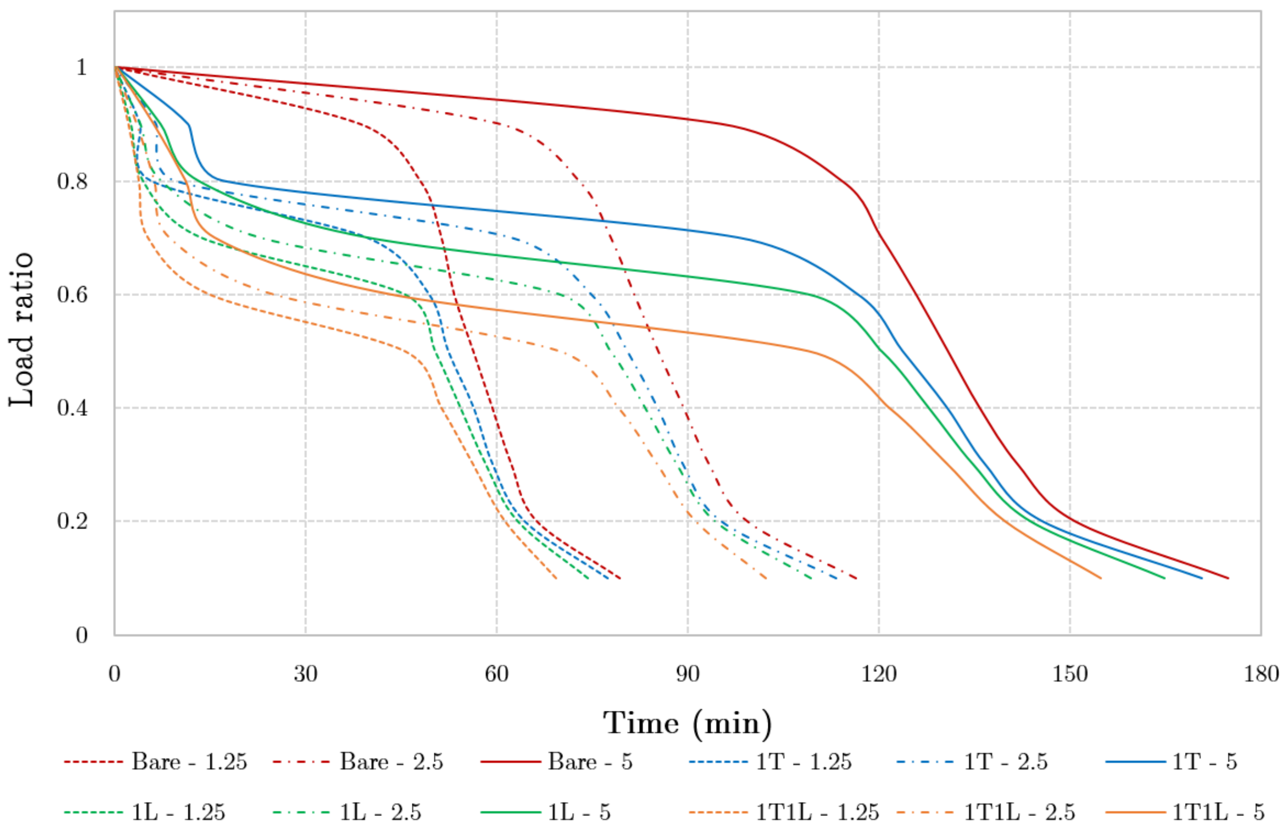

Load ratio
Time (min)
0
0.2
0.4
0.6
0.8
1
0
30
60
90
120
150
180
Bare - 1.25
Bare - 2.5
Bare - 5
1T - 1.25
1T - 2.5
1T - 5
1L - 1.25
1L - 2.5
1L - 5
1T1L - 1.25
1T1L - 2.5
1T1L - 5

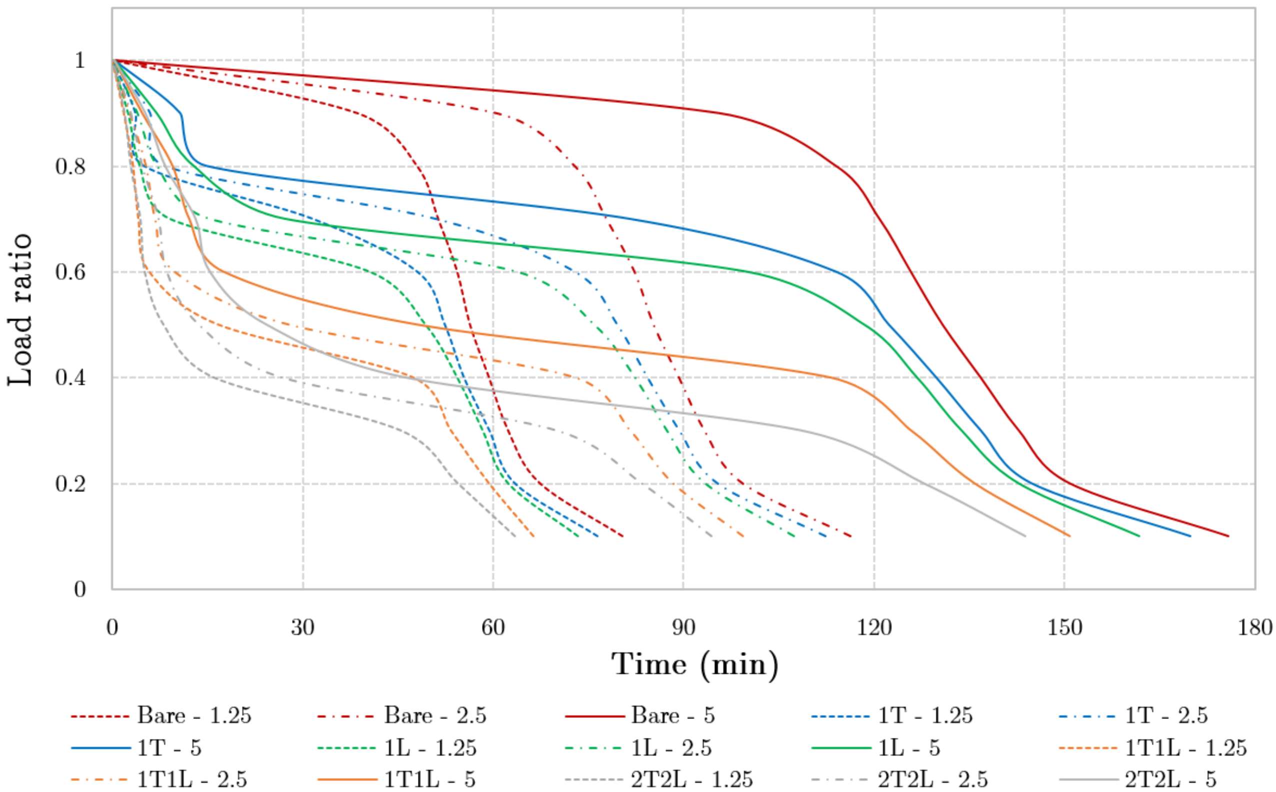
Load ratio
1
0.8
0.6
0.4
0.2
0
0
30
60
90
120
150
180
Time (min)
Bare - 1.25
Bare - 2.5
Bare - 5
1T - 1.25
1T - 2.5
1T - 5
1L - 1.25
1L - 2.5
1L - 5
1T1L - 1.25
1T1L - 2.5
1T1L - 5
2T2L - 1.25
2T2L - 2.5
2T2L - 5

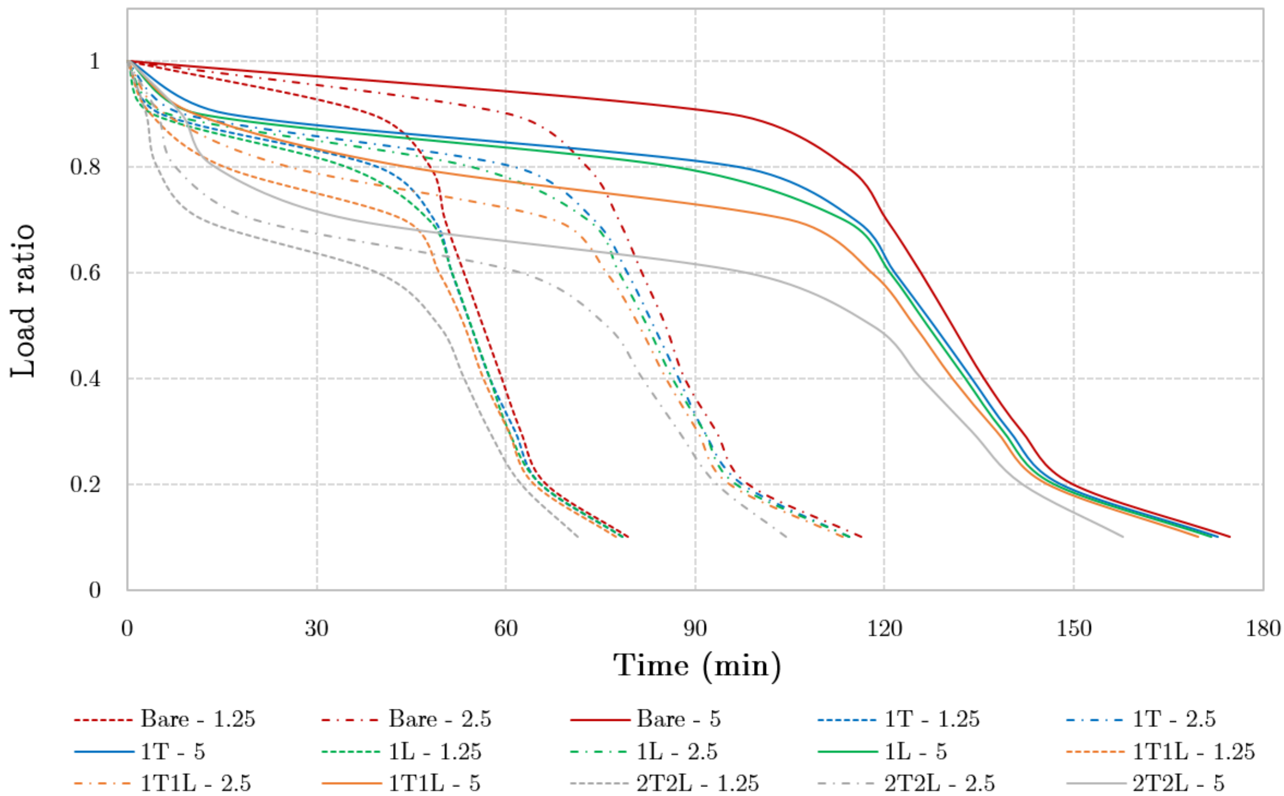

Load ratio
Time (min)
0
0.2
0.4
0.6
0.8
1
0
30
60
90
120
150
180
Bare - 1.25
Bare - 2.5
Bare - 5
1T - 1.25
1T - 2.5
1T - 5
1L - 1.25
1L - 2.5
1L - 5
1T1L - 1.25
1T1L - 2.5
1T1L - 5
2T2L - 1.25
2T2L - 2.5
2T2L - 5

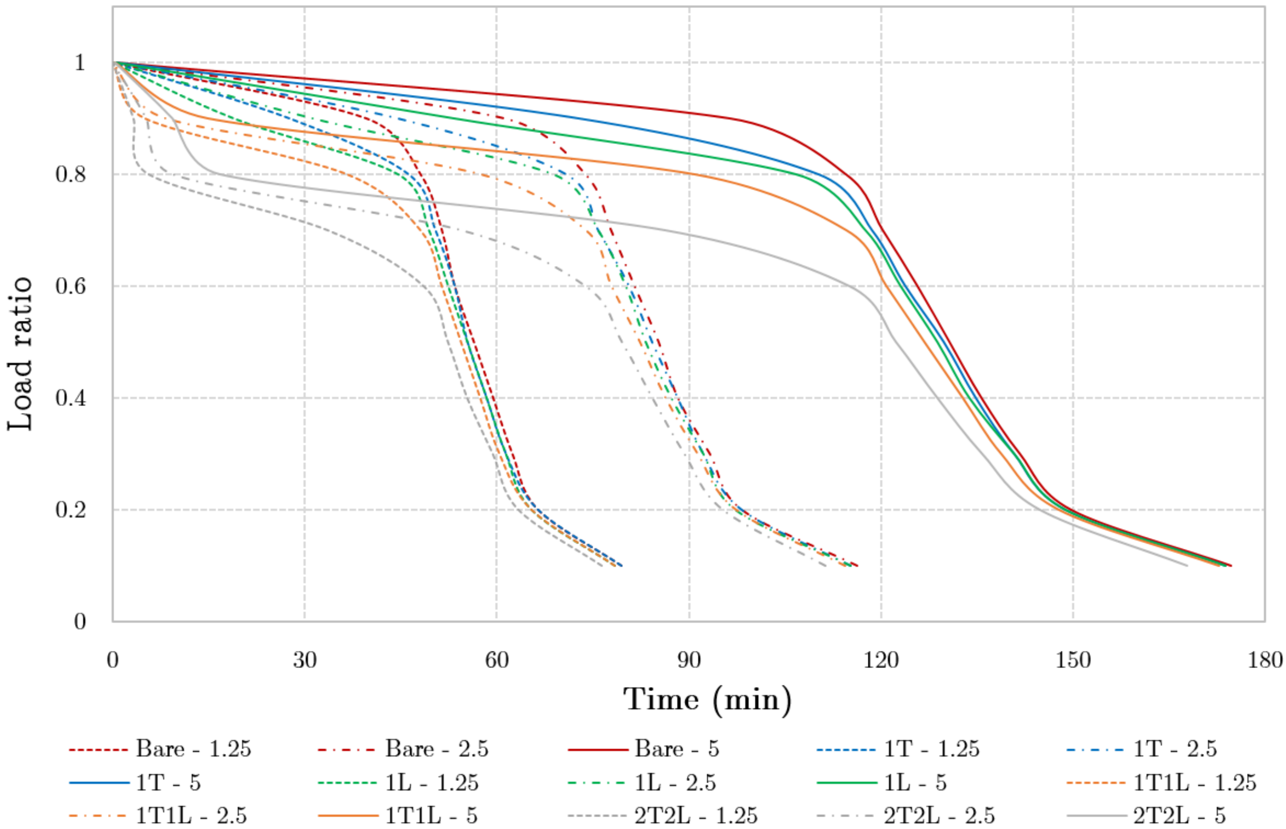

Load ratio
1
0.8
0.6
0.4
0.2
0
0
30
60
90
120
150
180
Time (min)
Bare - 1.25
Bare - 2.5
Bare - 5
1T - 1.25
1T - 2.5
1T - 5
1L - 1.25
1L - 2.5
1L - 5
1T1L - 1.25
1T1L - 2.5
1T1L - 5
2T2L - 1.25
2T2L - 2.5
2T2L - 5